Correspondence to:
M. Alberty,
malberty@princeton.edu

Moored Observations of Transport in the Solomon Sea

Marion Alberty[1] , **Janet Sprintall[1]** , **Jennifer MacKinnon[1]** , **Cyril Germineaud[2]** , **Sophie Cravatte[3]** , and **Alexandre Ganachaud[3]**

[1]Scripps Institution of Oceanography, University of California, San Diego, La Jolla, CA, USA, [2]Cooperative Institute for Marine and Atmospheric Studies, University of Miami and NOAA/AOML/Physical Oceanography Division, Miami, FL, USA, [3]Laboratoire d'Etudes en Géophysique et Océanographie Spatiales, Université de Toulouse, CNES, CNRS, IRD, UPS, Toulouse, France

Abstract The Solomon Sea is a marginal sea in the western Pacific warm pool that contains the South Pacific low latitude western boundary currents. These low latitude western boundary currents chiefly exit the Solomon Sea through three channels (Vitiaz Strait, St. George's Channel, and Solomon Strait) and serve as the primary source water for the Equatorial Undercurrent. Simulations have shown that transport partitioning between the straits determines the water mass structure of the Equatorial Undercurrent, but the relative contributions of transport through each strait have not been observed before. As part of the Southwest Pacific Ocean Circulation and Climate Experiment, an array of moorings was deployed simultaneously in the three outflow channels of the Solomon Sea from July 2012 until March 2014 to resolve transport and water properties in each strait. Above deep isopycnals ($\sigma_0 \leq 27.5$), Vitiaz and Solomon Straits account for 54.2% and 36.2% of the mean transport, respectively, with the remaining 9.6% exiting through St. George's Channel. The strongest subinertial transport variability is observed in Solomon Strait and dominates total Solomon Sea transport variability, and a significant fraction of this variability is at intraseasonal time scales. Finally, a previously unobserved deep current at 1,500-m depth is found to enter the Solomon Sea through Solomon Strait, with a deployment-mean transport of 4.6 Sv (Sv $\equiv 10^6$ m^3/s).

1. Introduction

The Solomon Sea contains the low latitude western boundary current (LLWBC) system of the South Pacific, which serves to connect the Equatorial Pacific and South Pacific subtropical circulations (Fine et al., 1994; Grenier et al., 2011, 2014; McCreary & Lu, 1994; Tsuchiya, 1968, 1989). Topography of the Solomon Sea restricts the LLWBC system to transit through three relatively deep channels: Vitiaz Strait, St. George's Channel, and Solomon Strait (Figure 1). This LLWBC system supplies approximately two thirds of the Equatorial Undercurrent (EUC) transport that reaches the Central Pacific (Grenier et al., 2011). Modeling studies (Grenier et al., 2011; Qin et al., 2016) show that the waters exiting equatorward through the three straits have distinct pathways to the EUC. Different transit times and mixing rates are associated with each pathway and influence the upper/lower and Northern/Southern Hemisphere structure of EUC water mass properties.

The relatively cold, iron-rich waters of the EUC upwell in the eastern Pacific, supporting an enhancement of primary production that has global significance (Pennington et al., 2006; Qin et al., 2016; Ryan et al., 2006). Given that iron is a limiting nutrient in equatorial Pacific primary productivity, the Solomon Sea has been identified as a region of interest. Sources of iron have been identified along the LLWBC pathways that pass through Vitiaz Strait and Solomon Strait (Labatut et al., 2014; Mackey et al., 2002; Radic et al., 2011; Slemons et al., 2010, 2012; Qin et al., 2016). Pathways with short transit times from the Solomon Sea to regions of upwelling in the eastern Pacific, such as through Solomon Strait, are more efficient at transporting iron and driving primary productivity (Qin et al., 2016), but until now, the relative contributions of the total volume transport through each strait have not been simultaneously observed. Direct observations of iron transport have still not been made in the Solomon Sea. However, quantifying the partitioning of volume transport between straits is key for understanding the influence of the different water mass pathways on equatorial primary productivity.

The Solomon Sea is also an important pathway for Antarctic Intermediate Water (AAIW) to travel from the South to North Pacific Ocean (Lindstrom et al., 1990; Qu & Lindstrom, 2002, 2004; Tsuchiya, 1991). AAIW
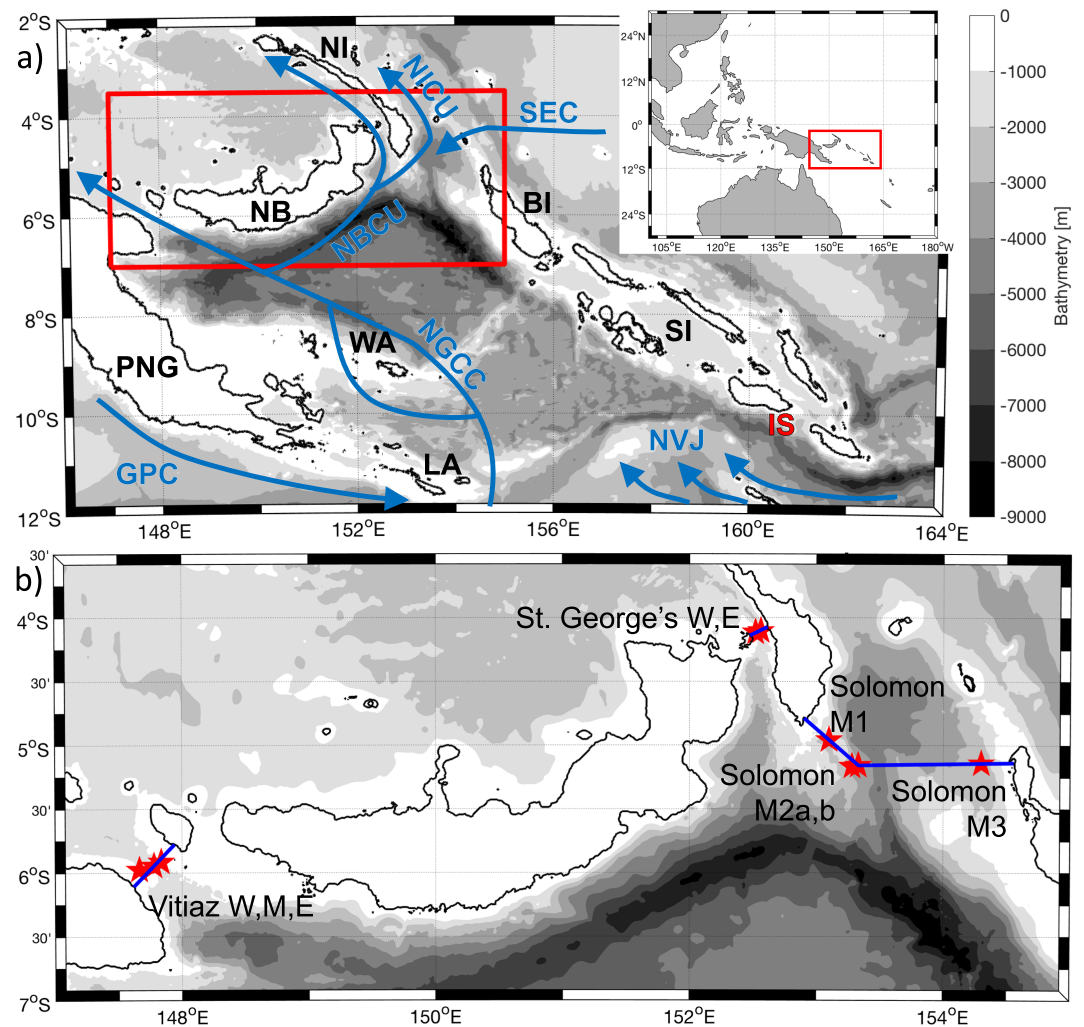
Figure 1. (a) Solomon Sea bathymetry and schematic of the major currents within the basin: Gulf of Papua Current (GPC), New Guinea Coastal Current system (NGCC), New Britain Coastal Undercurrent (NBCU), New Ireland Coastal Undercurrent (NICU), North Vanuatu Jet (NVJ), and South Equatorial Current (SEC). The main island of Papua New Guinea (PNG), New Britain (NB), New Ireland (NI), Woodlark Archipelago (WA), Louisiade Archipelago (LA), Bougainville Island (BI), and the Solomon Islands (SI) are noted, as is Indispensable Strait (IS). The regional location of the Solomon Sea within the Southwest Pacific is shown in the inset map. (b) The locations and names of the Southwest Pacific Ocean Circulation and Climate Experiment moorings (red stars and text) and the cross-strait transects used to calculate volumetric transport through each channel (blue lines). The map's location within the Solomon Sea is noted by the red box in (a).

that transits the Solomon Sea supplies both the North Equatorial Countercurrent (Reid Jr, 1965; Tsuchiya, 1991) and the Mindanao Undercurrent (Fine et al., 1994; Hu et al., 1991; Qu et al., 1998). The LLWBC system additionally delivers South Pacific lower thermocline and deep waters, including AAIW, to the Indian Ocean via the Indonesian Through Flow (Talley & Sprintall, 2005). Two synoptic observations suggest that AAIW transport through St. George's Channel and Solomon Strait combined is comparable to that through Vitiaz Strait (Germineaud et al., 2016). However, temporal variability is significant over the two seasons, leaving the importance of St. George's Channel and Solomon Strait in AAIW transport an open question.

The Climate and Ocean: Variability, Predictability and Change (CLIVAR) endorsed Southwest Pacific Ocean Circulation and Climate Experiment (SPICE) international program was designed in part to address the gap in our knowledge of Solomon Sea circulation through numerical modeling and in situ observations

(comprehensive reviews of the project and the ongoing activities are detailed in Ganachaud et al., 2014, and specifically for the Solomon Sea in Ganachaud et al., 2017). As part of SPICE, a cofunded, French-U.S. experiment for an 18-month mooring campaign was designed to quantify the total Solomon Sea transport and partition of transport that passes through Vitiaz Strait, St. George's Channel, and Solomon Strait. The study is unprecedented for the region in terms of the vertical resolution and temporal duration of velocity observations made simultaneously in each channel. Additionally, temperature and salinity sensors were deployed to investigate the water mass variability in the thermocline, intermediate, and deep layers.

Here we present the first simultaneous observations of transport from all three exit passages of the Solomon Sea acquired under the SPICE program. The contribution of each exit channel in the mean and the temporal variability are quantified over the deployment period. Section 2 provides background about the mean and variable current structure and associated water mass characteristics of the Solomon Sea. Section 3 details the moored SPICE observations and the procedure for converting the individual observations into a gridded, cross-channel data set. The mean and time-varying transport and partitioning between channels for each layer is detailed in section 4. A summary of the results and investigation into the relationships between layer transport and potential forcing mechanisms is given in section 5. The paper concludes with final remarks in section 6.

2. Solomon Sea Currents and Water Masses

2.1. Solomon Sea Geography

The Solomon Sea is bordered by the main island of Papua New Guinea to the West, the islands of New Britain and New Ireland to the North, and the Solomon Islands chain to the East (Figure 1a). The southern border is open to transport from the Coral Sea, while flow through the northern border is restricted to Vitiaz Strait (37 km wide at 250-m depth, 1,070-m sill depth), St George's Channel (15 km wide at 250-m depth, 1,400-m sill depth), and Solomon Strait (185 km wide at 250-m depth, 2,525-m sill depth). There are several narrow and shallow gaps between the Solomon Islands along the eastern side of the Solomon Sea, where surface layer transport is exchanged. A single deep channel, Indispensable Strait (50 km wide, 1,400-m sill depth), is the only potential location along the eastern boundary where thermocline and deeper waters can be transported into the Solomon Sea. Limited observations suggest the contribution is relatively small compared to inflow through the southern opening (2–3 Sv, ~10% of mean transport into Solomon Sea; Gasparin et al., 2012).

2.2. Surface and Thermocline Circulation

From the ocean surface to the base of the thermocline (σ_0=26.7, 350- to 420-m depth), mean circulation is supplied to the Solomon Sea by the Gulf of Papua Current (GPC; SPICE Community, 2012) from the southwest, the North Vanuatu Jet (NVJ) from the southeast, and the South Equatorial Current (SEC) from the northeast through Solomon Strait (Fine et al., 1994; Hristova & Kessler, 2012; Kessler & Cravatte, 2013; Figure 1a). The deep and narrow GPC enters the Solomon Sea after retroflecting around the Louisiade Archipelago, becoming the New Guinea Coastal Current/Undercurrent system (NGCC/NGCU) (Gasparin et al., 2012; Lindstrom et al., 1987; Sokolov & Rintoul, 2000). The shallower NVJ enters the Solomon Sea more broadly across the southern entrance and merges with the NGCC southeast of Woodlark Archipelago (Davis et al., 2012; Cravatte et al., 2011; Gasparin et al., 2012; Germineaud et al., 2016; Hristova & Kessler, 2012; Melet et al., 2010a).

As the NGCC approaches Woodlark Archipelago, surface water flows northwestward through the archipelago, while thermocline NGCC passes to the east of Woodlark Archipelago (Cravatte et al., 2011; Germineaud et al., 2016; Hristova & Kessler, 2012; Melet et al., 2010a; Melet et al., 2011). North of Woodlark, the NGCC remerges before bifurcating again south of New Britain with one branch flowing northwest and passing through Vitiaz Strait, while the remainder flows northeastward along the coast of New Britian (Cravatte et al., 2011). Murray et al. (1995) used moored velocity observations to estimate a deployment-mean, full-depth transport through Vitiaz Strait of 15.8 Sv (Sv $\equiv 10^6$ m^3/s) and found minimum transport in March 1992 and enhanced transport in August 1992. Additional transport observations at Vitiaz Strait by Butt and Lindstrom (1994) and Cravatte et al. (2011) along with other transport observations from the Solomon Sea are summarized in Table 1.

Table 1

Comparison of Previously Reported Mean Solomon Sea Observed Transport (Sv) and Time Mean Transport From the Mooring Observations Made During the SPICE Field Program (28 July 2012 to 4 March 2014) Calculated Over the Same Depth Ranges and Months as the Referenced Observation

Reference	Reference's time period	Reference's transport (Sv)	SPICE transport (Sv)	Depth range (m)
Vitiaz Strait:				
Butt and Lindstrom (1994)	May 1988	6.1±0.3	5.7±1.6	40–320
Murray et al. (1995)	1992–1993	14.9–19.0	12.4±3.3	0 to bottom
Cravatte et al. (2011)	1985–2007	7.4±2.6	6.5±1.8	20–300
Germineaud et al. (2016)	Jul/Aug 2012	19.4±0.4	18.7±5.0[a]	0–1,000
	Mar 2014	10.9±0.4	5.3±1.5[a]	0–1,000
St. George's Channel:				
Butt and Lindstrom (1994)	May 1988	3.1±0.2	2.3±0.4	40–300
Cravatte et al. (2011)	1985–2007	1.5±1.2	1.6±0.3	20–300
Solomon Strait:				
Cravatte et al. (2011)	1985–2007	4.2±1.9	4.5±0.5	20–300
St. George's Channel and Solomon Strait:				
Germineaud et al. (2016)	Jul/Aug 2012	18.8±2.3	24.6±2.1[a]	0–1,000
	Mar 2014	2.2±2.3	11.7±0.9[a]	0–1,000
Total Solomon Sea Transport:				
Sokolov and Rintoul (2000)	Jun/Jul 1993	26[b]	35.6±5.1	0 to bottom
Davis et al. (2012)	2007–2010	15–20	23.9±3.3	0–700
Gasparin et al. (2012)	Aug 2007	29±5	30.8±4.8	0–1,300
Zilberman et al. (2013)	2004–2011	18.7±1.4	25.0±3.5	0–1,000
Germineaud et al. (2016)	Jul/Aug 2012	36.2±2.6	43.2±5.4[a]	0–1,000
	Mar 2014	10.7±2.6	11.5±1.6[a]	0–1,000
Kessler et al. (2019)	2007–2016	20.2	23.9±3.3	0–700
Anutaliya et al. (2019)	2012–2017	15.2±6.8	20.5±2.8	0–500

Note. Positive values indicate equatorward transport out of the Solomon Sea. The associated uncertainties given for SPICE estimates reflect the uncertainty associated with the various interpolation and extrapolation schemes. See references for uncertainties associated with previously published values. SPICE = Southwest Pacific Ocean Circulation and Climate Experiment.
[a]The referenced observations are concurrent with the SPICE mooring deployment. SPICE estimates only use mooring observations that are from the same month and year as the reference time period.
[b]Only accounts for transport associated with the New Guinea Coastal Current system.

The portion of the current that travels eastward from the bifurcation point is referred to as the New Britain Coastal Undercurrent (NBCU; Figure 1a). The NBCU bifurcates south of New Ireland, and a portion of the flow exits the Solomon Sea through St. George's Channel, while the majority of NBCU transport exits through Solomon Strait (Fine et al., 1994; Melet et al., 2010a). The fraction of the NBCU that exits through Solomon Strait flows northward along the coast of New Ireland as the New Ireland Coastal Undercurrent (NICU; Cravatte et al., 2011). Mean transport exiting St. George's Channel is observed to be relatively small (1–3 Sv above 300 m; Table 1; Butt & Lindstrom, 1994; Cravatte et al., 2011), with modeled transport by Melet et al. (2011), suggesting a similarly small mean full-depth transport (2.5 Sv). Synoptic observations by Germineaud et al. (2016) find larger transports (4–8 Sv) and suggest significant temporal variability. However, no sustained observations have been made in St. George's Channel, and temporal variability of transport has not been resolved.

The SEC, which is relatively shallow (∼200 m deep) but extends into the upper thermocline, enters the Solomon Sea through Solomon Strait and travels westward toward Vitiaz Strait, joining the NGCC south of New Britain (Cravatte et al., 2011; Germineaud et al., 2016; Hristova & Kessler, 2012). Total transport through Solomon Strait thus depends on the balance between the outflowing NBCU and inflowing SEC. Cravatte et al. (2011) estimate a Solomon Strait mean transport of 4.4 Sv out of the Solomon Sea for 20- to 300-m depth, though estimates by Germineaud et al. (2016) suggest NBCU and SEC variability at seasonal time scales is significant with transports of 11 Sv in July/August 2012 and −2 Sv in March 2014 over the top 1,000 m (Table 1). While previous observations have expanded our understanding of the mean current pathways in the Solomon Sea, historical transport estimates have either not resolved all three straits (Butt & Lindstrom, 1994; Murray et al., 1995), provide only a snapshot of transport through the straits (Germineaud et al., 2016), or are limited to the top 300 m of the ocean (Cravatte et al., 2011).

The seasonal cycle of the surface circulation in the Solomon Sea is driven by monsoonal wind forcing and the annual migration of the South Pacific convergence zone (Hristova & Kessler, 2012). Meanwhile, seasonal thermocline variability is driven by linear Rossby waves forced by seasonal wind changes over the South Pacific (Kessler & Gourdeau, 2007; Kessler et al., 2019; Melet et al., 2010a). In austral summer, during the strong southeasterly trade season, the whole LLWBC system strengthens in the surface and thermocline layers both at the entrance and exits of the Solomon Sea, with differences in phasing ranging from June to November. This has been consistently shown in modeling (Kessler & Gourdeau, 2007; Kessler et al., 2019; Melet et al., 2010a) and observations (Cravatte et al., 2011; Hristova & Kessler, 2012; Melet et al., 2010b).

Interannual thermocline transport variability in the Solomon Sea is observed to be large with fluctuations of 10 Sv and is dominated by a response to El Niño-Southern Oscillation (ENSO) forcing (Anutaliya, Send, Sprintall, McClean, Lankhorst, & Koelling 2019; Davis et al., 2012; Kessler et al., 2010b, 2019; Melet et al., 2013). As no significant ENSO events occurred during the deployment period of 2012–2014 and interannual variability is observed to be relatively weak during this study period, interannual transport variability will not be discussed in detail. However, it is necessary to keep in mind that interannual transport variability can be significant when comparing transport estimates over different time periods, such as those summarized in Table 1.

2.3. Intermediate Circulation

Along intermediate isopycnals ($26.7 < \sigma_0 \leq 27.5$, ~400- to 1,400-m depth), water is transported by the NGCU system into the Solomon Sea in a narrow, strong current along the coast of Papua New Guinea (Gasparin et al., 2012; Germineaud et al., 2016; Melet et al., 2011; Qu & Lindstrom, 2002; Tsuchiya, 1991). Outside of the boundary current region, intermediate transport through the southern opening of the Solomon Sea is observed to be weak and variable between synoptic observations (Gasparin et al., 2012; Germineaud et al., 2016). Hydrographic observations indicate that the NGCU transports intermediate waters equatorward through Vitiaz Strait, supplying the North Pacific with intermediate waters up to 15°N (Germineaud et al., 2016; Tsuchiya, 1981; Qu & Lindstrom, 2004). Simulations by Melet et al. (2011) suggest that half of Solomon Sea intermediate water mass transport passes through Vitiaz Strait and that nearly all of Vitiaz Strait intermediate water transport comes from the southern opening of the Solomon Sea via the NGCU.

Simulations also indicate that less than 10% of the mean intermediate transport passes through St. George's Channel and approximately 40% exits through Solomon Strait (Melet et al., 2011). Two hydrographic surveys find that the magnitude of intermediate water mass transport through St. George's Channel and Solomon Strait combined is comparable to that through Vitiaz Strait; however, there is a significant difference in transport magnitude observed between the two time periods (Germineaud et al., 2016). Simulations by Melet et al. (2011) indicate that one third of intermediate transport through Solomon Strait is supplied by the NBCU, while the majority is due to recirculation of intermediate waters that entered through the eastern side of Solomon Strait before circulating within the Solomon Sea and exiting along the western side of the strait.

Observations by Murray et al. (1995) were the first to demonstrate the variability of the NGCU down to 800-m depth within Vitiaz Strait, with decreased intermediate transports in March 1992 and enhanced intermediate transports in August 1992. Seasonal variability at intermediate depths (700–800 m) of the NGCU system equatorward of Vitiaz Strait (2.5°S, 142°E) has also been observed by Kawabe et al. (2008) with strong, northwestward velocities of 14 cm/s in May–July and weak to reserving current velocities in November–February. Kawabe et al. (2008) also observed intermediate depth NGCU variability on interannual time scales related to the 1988–1999 La Niña. Intermediate transport estimates by Germineaud et al. (2016) from July/August 2012 are a factor of 2 larger than those observed in March 2014 for all channels, further indicating significant temporal variability of intermediate transports in the Solomon Sea. While water properties and synoptic surveys have illuminated the pathways of intermediate water masses through the Solomon Sea, the full-depth (400–1,300 m) intermediate total transport, partitioning, and temporal variability has not previously been observed.

Table 2
Mooring Deployment Information Including the Sill Depth for Each Strait, the Width of Each Strait at 250-m Depth, and Each Mooring's Location, Depth, and Deployment Period Based on the Dates of the Individual Moorings' Deployment and Recovery in UTC

Strait	Mooring	Location	Depth (m)	Deployment period
Vitiaz Strait	West	147°39.96′E 5°58.69′S	980	28/7/2012 to 14/3/2014
Sill: 1,070 m, Width: 37 km	Middle	147°46.68′E 5°56.64′S	1,130	28/7/2012 to 15/3/2014
	East	147°50.05′E 5°54.96′S	900	28/7/2012 to 13/3/2014
St. George's Channel	West	152°31.12′E 4°06.82′S	1,243	20/7/2012 to 7/3/2014
Sill: 1,400 m, Width: 15 km	East	152°33.86′E 4°06.17′S	1,433	20/7/2012 to 8/3/2014
Solomon Strait	M1 (West)	153°06.02′E 4°57.48′S	2,050	21/7/2012 to 6/3/2014
Sill: 2,525 m, Width: 185 km	M2a (Middle)	153°16.86′E 5°09.85′S	2,559	16/7/2012 to 6/3/2014
	M2b (Middle)	153°19.94′E 5°09.45′S	2,710	15/7/2012 to 6/3/2014
	M3 (East)	154°17.98′E 5°08.28′S	2,627	18/7/2012 to 4/3/2014

3. The SPICE Mooring Data Set

3.1. Mooring Deployment, Recovery, and Resulting Data Set

Nine subsurface moorings were deployed during the Pandora Cruise (cruise dates: 4 July to 1 August 2012) on the *R/V l'Atalante* and recovered during the MoorSPICE Cruise (cruise dates: 28 February to 31 March 2014) on the *R/V Thomas G. Thompson* resulting in a 19-month mooring time series (Figure 1b). The location, depth, and deployment period for each mooring is given in Table 2, in addition to the sill depth and channel width at 250-m depth for each channel. Locations and bottom depths are based on triangulation of the acoustic releases after the deployment during the Pandora cruise and were confirmed prior to recovery during MoorSPICE.

Multiple moorings were deployed in each channel to resolve the vertical and cross-strait temperature, salinity, and velocity structure and also for redundancy to ensure the experiment's success in the event of mooring failures. Moorings were typically equipped with an upward- and downward-looking Acoustic Doppler Current Profiler (ADCP) to resolve velocity in the upper part of the water column with additional single point current meters installed deeper along the line (Figures 2–4, black dots indicate mean location of velocity observations). This vertical resolution of sustained velocity observations is unprecedented for the Solomon Sea. Sensors measuring temperature, conductivity (which allows the estimation of salinity), and pressure were also deployed along the length of each mooring. The mooring pair in the center of Solomon Strait was the single exception, as M2a was the primary mooring with temperature, conductivity, and pressure sensors along the line and M2b was a redundant mooring with an upward-looking ADCP and measuring velocity and temperature from 50- to 1,700-m depth. All sensors were programmed to resolve the tides with sampling rates varying from every minute for some temperature sensors to every 2 hr for the deep current meters. A detailed description of the instrument settings and configuration along each mooring and the full quality control procedure is given in Alberty et al. (2017).

Three moorings (Vitiaz West, Middle, and East) were deployed across Vitiaz Strait with Vitiaz Middle deployed near the strait's sill in 1,130 m of water (Figure 1b). Two moorings (St. George's East and West) were deployed in St. George's Channel near the channel's sill. Four moorings (Solomon M1, M2a, M2b, and M3) were deployed across Solomon Strait with M1 deployed near the coast of New Ireland, M2a/M2b near the previously observed core of the NICU (Cravatte et al., 2011), and M3 near Bougainville Island. The mooring configuration at Solomon Strait was designed to both directly observe the velocity and estimate geostrophic transport using the observed temperature, salinity, and pressure from all three moorings.

Over the deployment period, the five moorings deployed in highly dynamic Vitiaz Strait and St. George's Channel sustained structural damage to varying degrees. While the cause of damage for each mooring is ultimately unknown, all five moorings displayed evidence of intense vibrations due to strong mean and tidal currents. Vitiaz Strait is also a highly trafficked channel due to both shipping and fishing. Both floats housing the upward and downward ADCPs for Vitiaz West and East were lost, leaving only the deep, single point current meters for those moorings. Vitiaz Middle sustained the loss of its topmost float reducing upper ocean vertical coverage of temperature and salinity but leaving ADCP velocity coverage unaffected. In St. George's Channel, both moorings sustained the loss of the topmost floats but retained their upward- and downward-
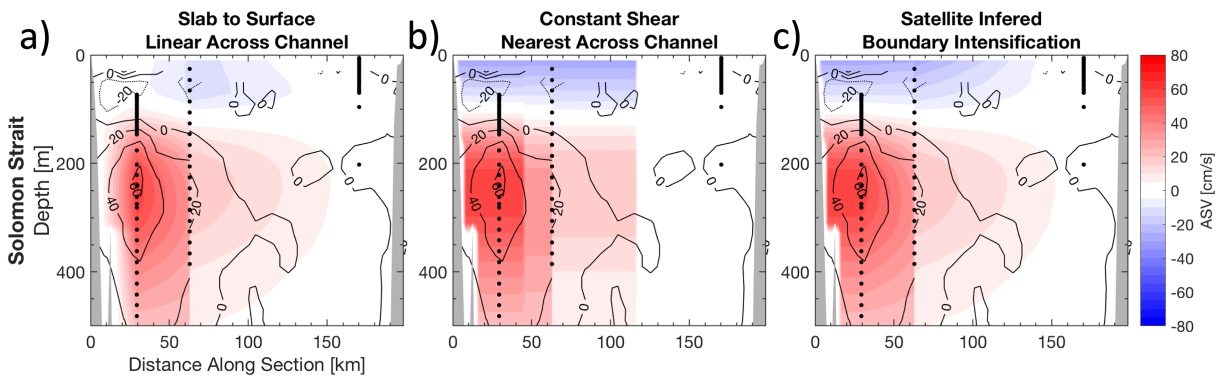
Figure 2. Example mean along-strait velocity (ASV; cm/s) cross sections from mooring observations using the (a) Slab to Surface and Linear Across Channel, (b) Constant Shear and Nearest Across Channel, or (c) Satellite Inferred and Boundary Intensification extrapolation models for the top 500 m of Solomon Strait. Mean shipboard Acoustic Doppler Current Profiler (ADCP) ASV sections are contoured at 20 cm/s intervals in black on all panels (solid lines are positive, and dotted are negative; see section A.4). The deployment-mean locations of all moored ADCP bins and single point current meters are indicated with black dots. Due to close vertical spacing of some ADCP bins, black dots may appear as thick vertical lines. Note the discontinuity across Solomon Strait is due to the discontinuous transect line used for the channel (Figure 1b).
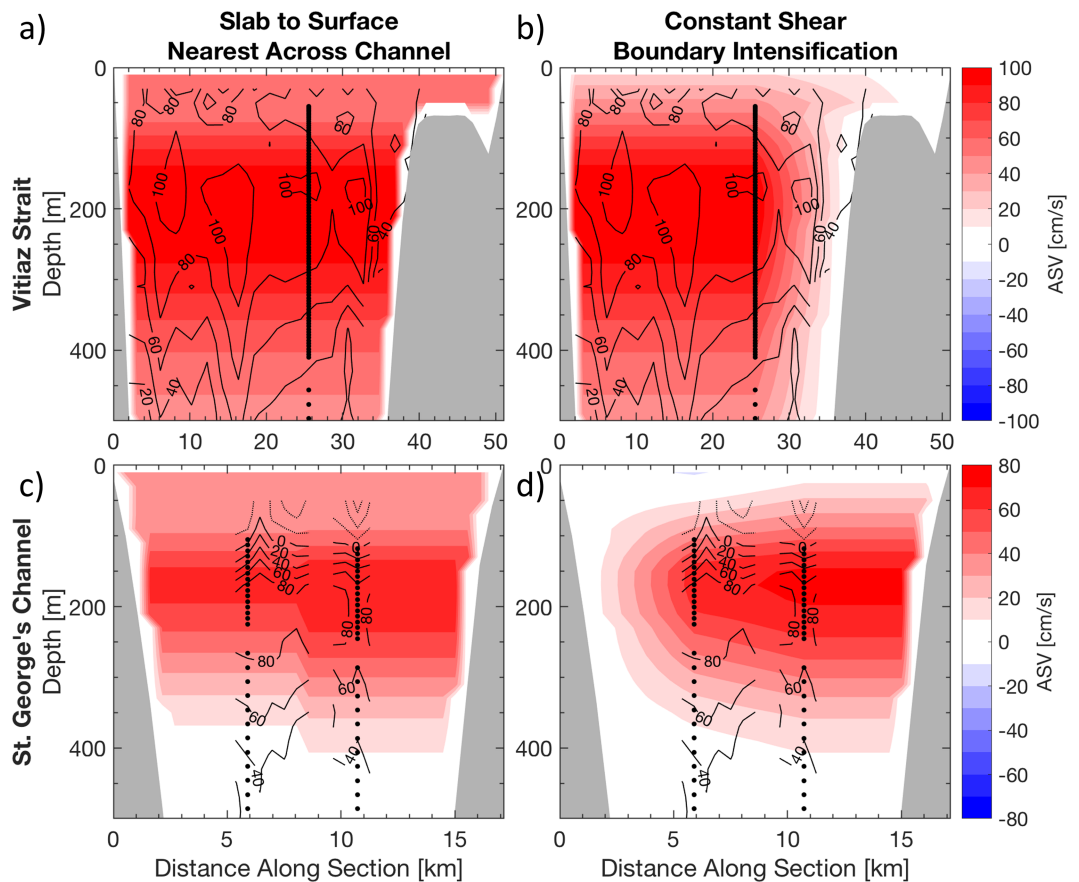

Figure 3. Example mean along-strait velocity (ASV; cm/s) cross sections from mooring observations using the (left) Slab to Surface and Nearest Across Channel and (right) Constant Shear and Boundary Intensification extrapolation models for the top 500 m of (a,b) Vitiaz Strait and (c,d) St. George's Channel. Mean shipboard Acoustic Doppler Current Profiler (ADCP) ASV sections are contoured at 20 cm/s intervals in black on all panels (solid lines are positive, and dotted are negative; see section A.4). The deployment-mean locations of all moored ADCP bins are indicated with black dots. Due to close vertical spacing of some ADCP bins, black dots may appear as thick vertical lines.
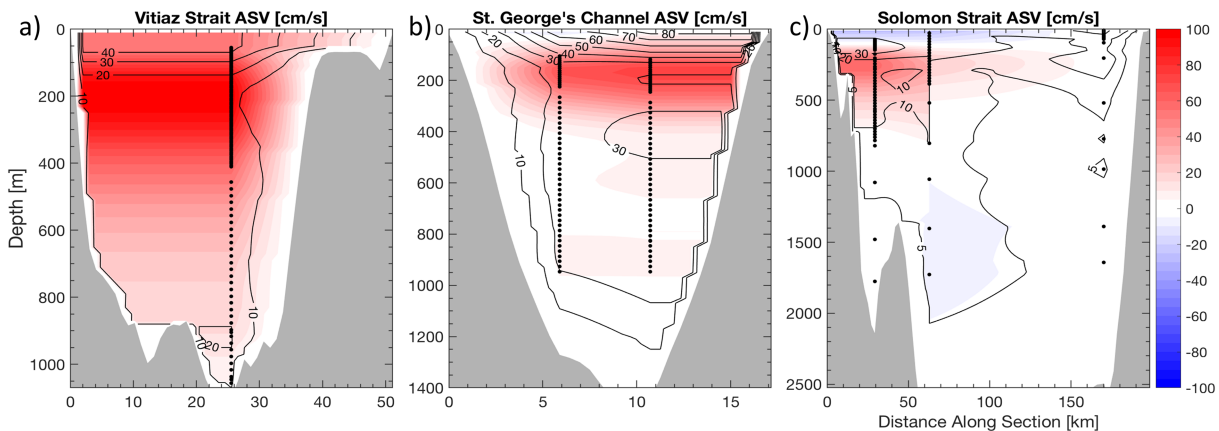
Figure 4. The mean (red-blue color map) and standard deviation (black contours) of the along-strait velocity (ASV; cm/s) for (a) Vitiaz Strait, (b) St. George's Channel, and (c) Solomon Strait. Statistics were calculated over the deployment period, and the vertical limits are the ocean surface to each channel's respective sill depth. Mean ASV sections are contoured at 5 cm/s increments, and red indicates transport exiting the Solomon Sea, while blue indicates transport entering. The standard deviation of the ASV is contoured in 10 cm/s intervals with an additional 5 cm/s contour for Solomon Strait. Deployment-mean locations of all ADCP bins and single point current meters are indicated with black dots for the directly observed velocity sections. Due to close vertical spacing of some ADCP bins, black dots may appear as thick vertical lines. Note the discontinuity across Solomon Strait is due to the discontinuous transect line used for the channel cross section (Figure 1b).

looking ADCPs, thus only reducing vertical coverage of temperature and salinity. All nine moorings were also subjected to significant blow over due to tidal and low-frequency currents.

At Solomon M2a, three Conductivity-Temperature-Depth (CTD) sensors at 300, 550, and 1,700 m failed at different times during the deployment period. The salinity record for the deepest sensor at 1,700 m was estimated from temperature observations at 1,700 m on Solomon M2b, using the tight relationship between temperature and salinity for this depth. A detailed description of this estimation procedure is given in section A.1. The CTDs at 300 and 550 m failed in October and April 2013, respectively, degrading the quality of the geostrophic transport estimate after April 2013. Nonetheless, the geostrophic transport estimate from the time period before the CTD failure is used to verify transport estimated by interpolating the in situ velocity across Solomon Strait. A description of the geostrophic transport estimate and comparison with transport estimated from the direct observations of velocity is given in sections A.2 and A.3.

After recovery, all data are quality controlled to treat for sensor drift, clock drift, and spurious values. Velocity observations are corrected for compass errors, converted from magnetic to earth coordinates taking magnetic declination into account, and unrealistic spikes and low quality ADCP velocity observations are removed. The full procedure is described in detail in Alberty et al. (2017). Quality-controlled data for each mooring are then filtered and interpolated onto a common, hourly time base.

Gridded 30-arc sec bathymetry and source identification data sets from both the General Bathymetric Charts of the Ocean (GEBCO) 2014 and W. H. Smith and Sandwell (1997) version 11 were investigated to determine the cross-sectional bathymetry and along-channel direction for the three straits. The along-strait direction for Vitiaz Strait (N50°W) is determined from a linear regression of the channel bathymetry near the mooring. The cross section for Vitiaz Strait is defined to be a line normal to the along-strait direction and passing through the location of Vitiaz Middle mooring (Figure 1b). The along-strait direction for St. George's Channel (N26°W) is defined as the direction normal to the cross section that passes through both St. George's West and East moorings. The along-strait directions for the moorings in Solomon Strait are defined to be the directions normal to the transects between adjacent moorings; N41°E for the cross section connecting M1 and M2 (Solomon Strait West) and N0° for M2 and M3 (Solomon Strait East). Cross-sectional bathymetry was interpolated onto each transect at 1-km resolution for Vitiaz and Solomon Straits and at 0.5 km for the narrower St. George's Channel. Channel bathymetry grid points based on in situ depth soundings accounted 66% and 20% of points for Vitiaz Strait and St. George's, respectively, when using GEBCO 2014 compared to 62% and 16% for W. H. Smith and Sandwell (1997). In Solomon Strait, 22% of channel grid points were based on soundings for W. H. Smith and Sandwell (1997), while 16% of points in the channel cross section were based on soundings for the GEBCO 2014 database. Thus, GEBCO 2014 bathymetry was

used for Vitiaz Strait and St. George's Channel, while W. H. Smith and Sandwell (1997) version 11 was used for Solomon Strait. Earth coordinate velocities (u,v) are rotated onto the local along-strait direction to calculate along-strait velocities (ASVs). Positive ASVs indicates flow that is exiting the Solomon Sea through the strait, while negative values indicate flow entering.

3.2. Vertical Interpolation and Extrapolation

At each time step, the available direct velocity observations are linearly interpolated onto a regular, vertical grid with 20-m spacing starting at 10-m depth. In other words, during a time step where there is a gap in the record of a current meter or ADCP bin, the vertical interpolation is done without that observation and thus with fewer points. If the gap is from the shallowest or deepest velocity observation, the vertical extent of the interpolated velocity profile is reduced. The strong and persistent currents imparted significant drag on the moorings, causing mooring blow over and reducing upper ocean instrument coverage. In Vitiaz Strait and St. George's Channel, on average, the top 55 m and 100 m of the water column, respectively, were beyond the range of the upward-looking ADCPs due to this persistent draw down (Figure 3, black dots). Mooring draw down was strongest during May–July in Vitiaz Strait and during April–July in St. George's Channel. Near-surface coverage of directly observed velocities varied across Solomon Strait with, on average, the top 70 m unresolved at Solomon M1 near the NICU core but only the top 25 and 5 m unresolved at Solomon moorings M2 and M3 where currents were weaker (Figures 2a–2c, black dots). Mooring draw down was strongest in September–December for Solomon M1.

Three models were tested to estimate the unresolved near-surface velocities at each time step:

1. *Slab to Surface.* The value of the shallowest observed velocity is assigned to all unresolved depths above that observation (Figures 2a, 3a, and 3c).
2. *Constant Shear.* Velocities are linearly extrapolated to the surface using the shallowest observed shear and velocity (Figures 2b, 3b, and 3d).
3. *Satellite Inferred.* The in situ velocity profile (u,v) is assumed to be the sum of the geostrophic velocity (u_g,v_g) and the surface Ekman velocity:

$$u = u_g + \frac{\sqrt{2}}{fd} e^{z/d} [\tilde{\tau}^x \cos(z/d - \pi/4) - \tilde{\tau}^y \sin(z/d - \pi/4)], \tag{1}$$

$$v = v_g + \frac{\sqrt{2}}{fd} e^{z/d} [\tilde{\tau}^x \sin(z/d - \pi/4) + \tilde{\tau}^y \cos(z/d - \pi/4)]. \tag{2}$$

The surface Ekman portion of the velocity is estimated at the mooring location where f is the local Coriolis frequency and $d \equiv \sqrt{2A/|f|}$ is the surface Ekman layer thickness that depends on the turbulent viscosity in the surface layer, A. The turbulent viscosity was estimated using the empirical relationship derived by Santiago-Mandujano and Firing (1990) and is a function of wind speed. The Cross-Calibrated Multiplatform (CCMP) surface vector winds (6-hr and 1/4° resolution; Atlas et al., 2011; Wentz et al., 2015) were interpolated onto the mooring's time and location and used to estimate A and the kinematic wind stress, $\tilde{\tau} \equiv \tau/\rho_0$, where the reference density, $\rho_0 = 1,019$ kg/m^3, was estimated using the mean surface density from shipboard CTD profiles (Ganachaud et al., 2017; Germineaud et al., 2016). For observed CCMP winds, the Ekman thickness was typically ~20 m in Solomon Strait. The estimated surface Ekman velocities are removed from the directly observed velocity profile. Absolute geostrophic surface velocities estimated from the SSALTO/DUACS Delayed-Time Level-4 sea surface height product (daily and 1/4° resolution) are interpolated onto the mooring's time and location. A linear interpolation is then applied from the mooring's shallowest velocity observation to the interpolated absolute geostrophic surface velocity. The estimated surface Ekman profile is then added back to the geostrophic profile (Figure 2c).

The surface models were chosen to reflect the variety of near-surface velocity structure resolved in prior synoptic observations or to take advantage of concurrent satellite observations. As the Slab to Surface and Constant Shear models do not require independent observations, these methods are applied to all moored velocity records. The satellite inferred method only applied to moorings in Solomon Strait where the strait is wide and moorings are located 30 km or farther from the coast to limit the effect of coastal contamination of the altimeter observations. Nonetheless, unquantified uncertainties are likely present in the satellite-based surface geostrophic velocities.

Vertical gaps in velocity observations are also present between the deepest observation and the channel bottom or sill depth. Near-bottom coverage is best in Vitiaz Strait where the deepest velocity observations are on average within 20 m of the sill depth. In St. George's Channel, on average, 450 m of the water column above the sill depth was not resolved. The deepest velocity observations in Solomon Strait were at a mean depth of 1,700 m for all three moorings, 825 m above the sill depth.

Two simple models are tested to estimate the unresolved velocities between the deepest observation and the bottom or sill depth:

1. *Slab to Bottom.* The value of the deepest observed velocity is assigned to all unresolved depths below that observation above the bottom or sill depth, whichever is the shallowest.
2. *Linear to Bottom.* Velocities are linearly interpolated from the deepest observation to zero velocity at the bottom or sill depth, whichever is the shallowest.

For either bottom models, the velocity in the grid space nearest the bottom or at the sill depth is always set to zero, assuming a no-slip boundary. The Slab to Bottom scheme gives an upper bound to transport estimates and resembles near-bottom velocity structure previously observed in Vitiaz Strait. The Linear to Bottom scheme results in conservative transport estimates and may be more realistic for Solomon Strait near-bottom velocity structure. The combination of these surface and bottom extrapolation models resulted in multiple gridded data sets for each mooring.

Velocities with inertial and super-nertial frequencies (periods < 7 days) are responsible for 16–53% of the observed velocity variance at the different moorings. Variance at tidal harmonics, in particular, accounts for one third to one half of the observed superinertial variance. Variability at these frequencies is generally the result of the barotropic tide and internal wave field. While a significant portion of kinetic energy at each mooring is contained in the inertial and superinertial frequencies, the processes responsible for these velocity variations are beyond the scope of this paper. Thus, for our purposes of estimating large-scale transports, all mooring ASV time series are low-pass filtered to only contain the subinertial frequencies (periods longer than 7 days).

3.3. Cross-Passage Interpolation and Extrapolation Schemes

Lateral interpolation of ASV between moorings and extrapolation of ASV to the sidewalls were carried out using three schemes:

1. *Linear Across Chanel.* ASV is linearly interpolated between moorings and to zero at the sidewalls for each depth (Figure 2a).
2. *Nearest Across Channel.* ASV is uniformly assigned across each depth in the channel by the nearest mooring observation (Figures 2b, 3a, and 3c).
3. *Boundary Intensification.* In Solomon Strait and Vitiaz Strait, the observed ASV at the westernmost mooring is assigned across each depth from that mooring to the western boundary (Figures 2c and 3b). In St. George's Channel, the observed ASV at the easternmost mooring is assigned across each depth from that mooring to the eastern boundary (Figure 3d). ASV is linearly interpolated between moorings and to zero for the remaining sidewalls.

The cross-channel interpolation schemes were chosen to approximate the different cross-channel velocity sections resolved in prior synoptic observations. For all models, ASVs in the bins nearest the sidewall boundary are set to zero, assuming a no-slip boundary condition. The lateral griding is done with 1-km spacing for Vitiaz Strait and Solomon Strait and with 0.5-km spacing for the narrower St. George's Channel. Due to the mooring configuration across Solomon Strait, ASV is laterally interpolated over two cross sections: Solomon Strait West from New Ireland to Solomon M2 and Solomon Strait East from Solomon M2 to Bougainville Island (Figure 1b).

3.4. Transport and Sensitivity

Transport (Sv) is estimated by integrating the gridded cross section of ASV over the cross-channel area. To investigate the vertical distribution of transport, the gridded cross sections of ASV are integrated across the cross-sectional width at each depth and reported as transport per unit depth (Sv/km). For all transport estimates, positive values indicate transport that is out of the Solomon Sea through the strait, and negative values indicate transport into the Solomon Sea.

Table 3
Summary of Deployment Mean Transport ± the Error Due to Interpolation Choices (and Mean Standard Deviation; Sv) and Mean (and Standard Deviation) of Transport (Sv) for the "Most Realistic" Choices for Vitiaz Strait, St. George's Channel, Solomon Strait, and the Sum of All Three Channels

Vertical bounds	Vitiaz Strait	St. George's Channel	Solomon Strait	Total
Mean transport from all choices				
$z \leq 100$ m	1.6±0.5 (1.6)	0.3±0.2 (0.6)	−1.4±0.5 (2.1)	0.5±0.7 (2.8)
$z{>}100$ m and $\sigma_0{<}26.7$	6.7±1.8 (0.9)	1.5±0.2 (0.7)	7.9±0.6 (3.4)	16.1±1.9 (3.6)
$26.7 \leq \sigma_0{<}27.5$	4.0±1.1 (2.1)	0.4±0.0 (1.8)	1.8±0.2 (5.3)	6.2±1.1 (6.0)
$\sigma_0{<}27.5$	12.4±3.3 (3.8)	2.2±0.3 (2.9)	8.3±0.9 (8.6)	22.8±3.5 (9.9)
$\sigma_0 \geq 27.5$	n/a	n/a	−4.6±1.0 (5.5)	−4.6±1.0 (5.5)
"Most realistic" transport				
$z \leq 100$ m	1.9 (1.4)	0.2 (0.8)	−1.8 (1.9)	0.3 (2.5)
$z{>}100$ m and $\sigma_0{<}26.7$	7.2 (1.0)	1.6 (0.8)	8.2 (3.5)	17.0 (3.7)
$26.7 \leq \sigma_0{<}27.5$	4.4 (2.2)	0.4 (1.7)	1.9 (5.4)	6.7 (6.1)
$\sigma_0{<}27.5$	13.5 (3.9)	2.1 (3.0)	8.3 (8.6)	24.0 (9.9)
$\sigma_0 \geq 27.5$	n/a	n/a	−5.4 (6.6)	−5.4 (6.6)

Note. For the "most realistic" transport estimates, Linear to Bottom and Boundary Intensification are used for all three channels and the surface extrapolation choice for each channel is Slab to Surface for Vitiaz Strait, Constant Shear for St. George's Channel, and Satellite Inferred for Solomon Strait.

While flow in Solomon Strait is observed to have a Rossby number less than one and should be well approximated by geostrophy, instrument failures in the latter half of the record degrade the quality of a geostrophic transport estimate, particularly in the thermocline. Transport estimated from in situ velocity observations is in good agreement with a geostrophic estimate before instrument failure and is utilized to estimate transport through Solomon Strait for the remainder of this manuscript (section A.3).

A summary of the deployment-mean transport, error, and mean standard deviation for all three channels over different vertical limits is given in Table 3. Due to the different interpolation and extrapolation choices, multiple transport time series were generated for each channel: 12 each for Vitiaz Strait and St. George's Channel and 18 for Solomon Strait. Mean transports are given as the average of the array of mean transports that result from the combination of different models. The transport error is the standard deviation of the mean due to the range of transport estimates from the different models. Table 4 summarizes the transport sensitivity due to all the interpolation and extrapolation choices for this experiment. The sensitivity of total channel transport to each interpolation choice is given as the average percent change in deployment-mean transport as a result of using Choice A rather than Choice B. Percent change is calculated for pairs of time series where all extrapolation choices are identical except for the choice of interest. The percent change from all the pairs are averaged to give the sensitivity of transport in each channel to the different extrapolation choices.

An in-depth discussion comparing the different interpolation and extrapolation schemes with prior observations and investigating the sensitivity of transport estimates is given in sections A.4 and A.5. The following is a *brief* summary of that discussion.

For Vitiaz Strait and St. George's Channel, transport estimates are sensitive to the cross-channel extrapolation model and relatively insensitive to vertical extrapolation choices (Table 4). In Vitiaz Strait, the Slab to Surface and Linear to Bottom schemes reproduce observed ASV patterns, while the Linear to Surface and

Table 4
Total Channel Transport Sensitivity Due to Different Interpolation and Extrapolation Schemes Represented as the Average Percent Change in Mean Total Channel Transport When Using the First Scheme Listed Rather Than the Second

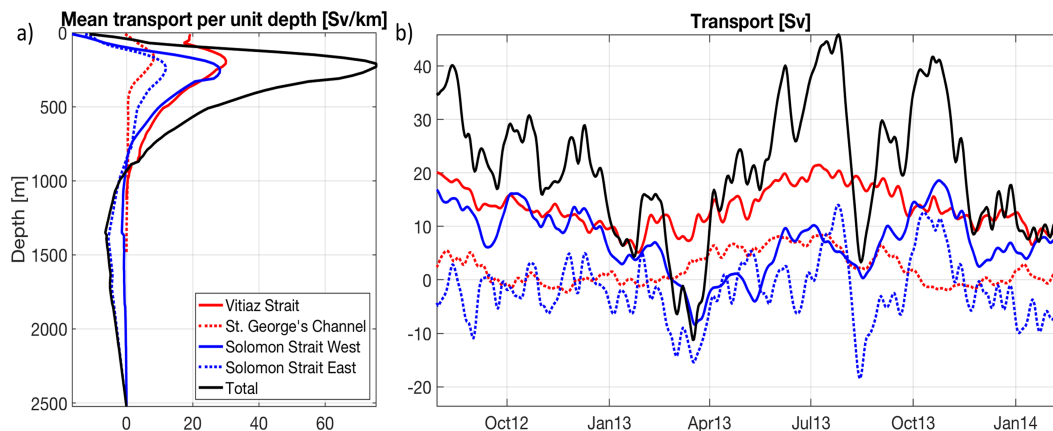| Extrapolation scheme	Vitiaz Strait	St. George's Channel	Solomon Strait
Constant shear vs. slab to surface	−3.7%	−9.6%	−36.6%
Constant shear vs. satellite inferred	n/a	n/a	−0.9%
Linear to bottom vs. slab to bottom	0.0%	−0.6%	43.2%
Linear vs. nearest across channel	−94.0%	−42.4%	−41.6%
Linear across channel vs. boundary intensification	−63.5%	−24.2%	−55.5%

Figure 5. (a) Mean profiles of subinertial transport per unit depth (Sv/km) and (b) the surface to sill depth subinertial transport time series (Sv) for Vitiaz Strait (solid red line), St. George's Channel (dotted red line), Solomon Strait West (solid blue line), Solomon Strait East (dotted blue line), and the total of the three straits (solid black line).

Linear to Bottom provide reasonable estimates in St. George's Channel (Figure 3). Mean shipboard ADCP (SADCP) sections and prior observations indicate that the Boundary Intensification scheme is an appropriate choice for both channels.

Transport in Solomon Strait, however, is sensitive to nearly all interpolation choices and methods (Table 4). Independent observations indicate that the Constant Shear or Satellite Inferred surface models best approximate near-surface ASV in Solomon Strait (Figure 2). The Satellite Inferred surface extrapolation is preferred as it is the most physically based model. While total transport in Solomon Strait is sensitive to the bottom scheme, there are no published observations of ASV below 1,000 m in the channel. The Linear to Bottom scheme is chosen as it gives conservative estimates of deep transport through Solomon Strait. Prior observations and simulations indicate that the Boundary Intensification scheme is the most representative choice for cross-channel interpolation in Solomon Strait (Figure 2).

The above choices, which we consider to be the "most realistic" for each channel, are used to visualize the mean and temporal variability of each channel's transport in the remaining figures of this paper. All discussion of the remaining figures is thus focused on the structure or temporal variability indicated by these most realistic cases. The deployment-mean transports and standard deviations of transport due to temporal variability over different vertical limits for these most realistic cases are also summarized in Table 3. The deployment-mean transports for each strait and the Solomon Sea listed in section 4.1 are from the average of all cases and are used to determine mean transport partitioning. Both error estimates and average standard deviations due to temporal variability are given for these mean transport estimates to help distinguish them from transport estimates from the most realistic cases.

4. Results: Transports and Partitioning

4.1. Mean Transport and Partitioning

During the SPICE mooring deployment (28 July 2012 to 4 March 2014), over half (54.2%) of the total Solomon Sea transport above the base of AAIW (σ_0=27.5, ~1,400-m depth) exits through Vitiaz Strait. Vitiaz Strait has a mean transport of 12.4±3.3 Sv, and flow is relatively steady in time with an average standard deviation of 3.8 Sv. Deployment-mean transport through Vitiaz Strait is slightly less than previous synoptic observations when integrated over the same vertical limits (Table 1; Butt & Lindstrom, 1994; Germineaud et al., 2016), though not significantly different when compared to historical means (Cravatte et al., 2011; Murray et al., 1995). Mean Vitiaz Strait ASV and transport per unit depth are positive, out of the Solomon Sea, at all depths (Figures 4a and 5a, solid red line). ASV increases from 50 cm/s at the surface to 100 cm/s at 200 m and then decreases to the sill, where it still flows at 8 cm/s. This is consistent with the findings of Cravatte et al. (2011) and with Murray et al. (1995), who also reported ASV of 10–20 cm/s below 800-m depth.

St. George's Channel supplies a smaller fraction (9.6%) of the total Solomon Sea transport for σ_0<27.5 with a mean transport of 2.2±0.3 Sv and an average standard deviation of 2.9 Sv. Mooring transport estimates are in

agreement with previous mean transport estimates (Table 1; Cravatte et al., 2011), and prior synoptic observations fall within the observed temporal variability (Butt & Lindstrom, 1994). Mean surface currents are estimated to be near zero above the eastern mooring and −12 cm/s over the western mooring (Figure 4b). Mean transport per unit depth in St. George's Channel has a subsurface maximum of 8 Sv/km at 170-m depth associated with the NBCU (Figure 5a, dotted red line), which has a mean ASV of 73 cm/s at St. George's East (Figure 4b). The deployment-mean ASV decreases to less than 5 cm/s below 400-m depth, resulting in mean transport per unit depth of less than 1 Sv/km from 400 m to the sill depth. On average, ASVs observed at St. George's East are 5 cm/s stronger than those observed at St. George's West. Mean ASV in the NBCU is 20 cm/s stronger in the mooring observations compared to the mean SADCP sections of Cravatte et al. (2011). No prior observations have resolved ASV below 400 m within St George's Channel.

The remaining 36.2% of transport above the σ_0=27.5 isopycnal exits through Solomon Strait (8.3$\pm$0.9 Sv). Solomon Strait has the largest temporal variability with a standard deviation of 8.6 Sv. Previous estimates of mean transport in Solomon Strait are in agreement with the directly observed ASV estimate (Table 1; Cravatte et al., 2011). Transport in the top 100 m enters the Solomon Sea with 29.0 Sv/km of transport per unit depth at the surface (Figure 5a, blue lines). Both sides of Solomon Strait contribute nearly equally to the surface transport, but surface velocities are stronger on the western side of Solomon Strait with mean ASV of −28 cm/s above Solomon M1 and −26 cm/s above Solomon M2 (Figure 4c). Even with weaker surface ASV on the eastern side, the larger cross-sectional width results in comparable transport to the western side.

From 100- to 850-m depth, transport exits the Solomon Sea across Solomon Strait. Subsurface transport is maximum at 250-m depth for both the western and eastern sides with mean transports per unit depth of 28 and 12 Sv/km, respectively (Figure 5a, blue lines). This subsurface maximum in transport is associated with the outflowing NICU that has a mean ASV of 58 cm/s on the western side of the strait at Solomon M1 (Figure 4c). While the sill depth of both Vitiaz Strait (1,070 m) and St. George's Channel (1,400 m) are shallower than or nearly equal to the depth of the σ_0=27.5 isopycnal, Solomon Strait has a deeper sill depth of 2,525 m. At Solomon Strait, a transport of −4.6$\pm$1.0 Sv with a standard deviation of 5.5 Sv is observed *entering* the Solomon Sea between the σ_0=27.5 isopycnal and sill depth. A weak and broad inflow below 850 m is observed across all three moorings with the strongest mean ASV of 8 cm/s observed at Solomon M2. These are the first direct observations of this deep current.

The structure of mean ASV across Solomon Strait is in reasonable agreement with simulated circulation by Djath et al. (2014), including the persistent, deep inflow below 850-m depth. Simulations by Melet et al. (2010a) predict a weak thermocline level inflow at 200-m depth on the eastern side of Solomon Strait. Periodic inflows at thermocline depth are observed on the eastern boundary of Solomon Strait by mooring M3, as is indicated by the elevated standard deviation of ASV from the surface to 350-m depth. However, a mean inflow predicted by simulations at that location is not resolved or confirmed by these mooring observations (Figures 4c and 4d).

The mean total transport for all three exit straits combined from the surface to the base of AAIW (σ_0=27.5) is 22.8$\pm$3.5 Sv equatorward, out of the Solomon Sea with an average standard deviation of 9.9 Sv due to temporal variability. The Solomon Sea mooring deployment-mean total transport is an overestimate when compared to other multiyear estimates (Table 1). While these differences are not statistically significant for the SPICE estimates compared to those of Kessler et al. (2019) or Anutaliya et al. (2019), there are statistically significant differences when compared to Davis et al. (2012) and Zilberman et al. (2013). A potential source of this difference may be the strong interannual variability, on the order of 10 Sv, observed by both Anutaliya et al. (2019) and Kessler et al. (2019) in the Solomon Sea. This strong interannual variability and the different time ranges of the SPICE observations compared to Davis et al. (2012) and Zilberman et al. (2013) may contribute to the difference. An additional point worth noting is that the Argo network in the Solomon Sea was relatively sparse during the study period of Zilberman et al. (2013) and did not resolve transport close to the western boundary.

Transport above 50-m depth is near zero, as in-flowing transport through Solomon Strait and partially balanced by outflowing Vitiaz Strait surface transport (Figure 5a). From 50- to 950-m depth, 26.5 Sv is transported equatorward and out of the Solomon Sea with maximum of 75 Sv/km transport per unit depth around 220 m. While subsurface transport maxima from all three channels contribute to the total Solomon Sea
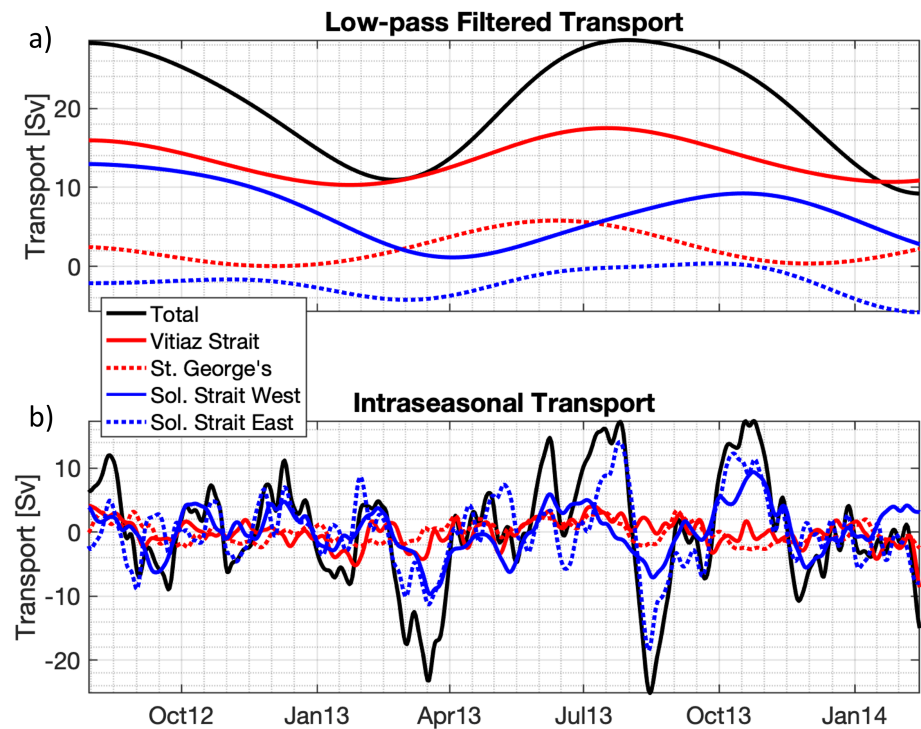
Figure 6. (a) Half-year low-pass filtered and (b) intraseasonal surface to sill depth transport (Sv) for Vitiaz Strait (solid red line), St. George's Channel (dotted red line), Solomon Strait West (solid blue line), Solomon Strait East (dotted blue line), and the total of the three straits (solid black line).

transport, Solomon Strait contributes the largest fraction of mean thermocline transport (48.2%) with a slightly smaller contribution by Vitiaz Strait (42.4%; Table 3). Below the thermocline to 950-m depth, Vitiaz Strait and Solomon Strait West carry nearly equal fractions of mean intermediate transport. Mean total Solomon Sea transport reverses again below 950 m with weak flow down to 2,525-m depth that is into the Solomon Sea, entirely contributed by 5.6 Sv of transport from Solomon Strait East. South and upstream of the straits, Davis et al. (2012) and Zilberman et al. (2013) find mean profiles of transport per unit depth with similar vertical structure and subsurface maxima of ∼50 Sv/km at 250 m.

4.2. Time-Varying Transports

Top to bottom transport from the sum of the three channels ranges from −11.2 to 45.9 Sv over the deployment period (Figure 5b, solid black line). Visually, it is clear that Solomon Sea transport varies over a range of time scales with different contributions of temporal variability from different channels. Vitiaz Strait, St. George's Channel, and Solomon Strait West all exhibit variability at seasonal time scales, while Solomon Strait East displays large intraseasonal variations.

To tease apart the variance associated with seasonal and intraseasonal time scales, total Solomon Sea and channel transport time series are low-pass filtered with a half-year cut-off to estimate transport variability at seasonal time scales (Figure 6a). The low-pass filtered estimate is removed from the unfiltered transport (Figure 5b) to estimate the intraseasonal part of the transport signal (Figure 6b). Transport changes on seasonal time scales will be discussed first followed by a brief discussion of the intraseasonal variability.

The relative phasing of transport variability over the water column is most clear in the transport per unit depth anomaly (Figure 8), which is the transport per unit depth time series (Figure 7) with the mean profile of transport per unit depth removed (Figure 5a).

4.2.1. Seasonal Time Scale Variability

In Vitiaz Strait, the low-pass filtered transport remains positive over the deployment period with a mean of 12.4 Sv and is relatively steady in time with a standard deviation of 2.3 Sv (Figure 6a, solid red line). The persistent NGCU core in Vitiaz Strait, located between 100- and 300-m depth (Figure 7a), contributes significantly to this positive low-pass filtered time series. In-phase, strengthening and weakening of surface and
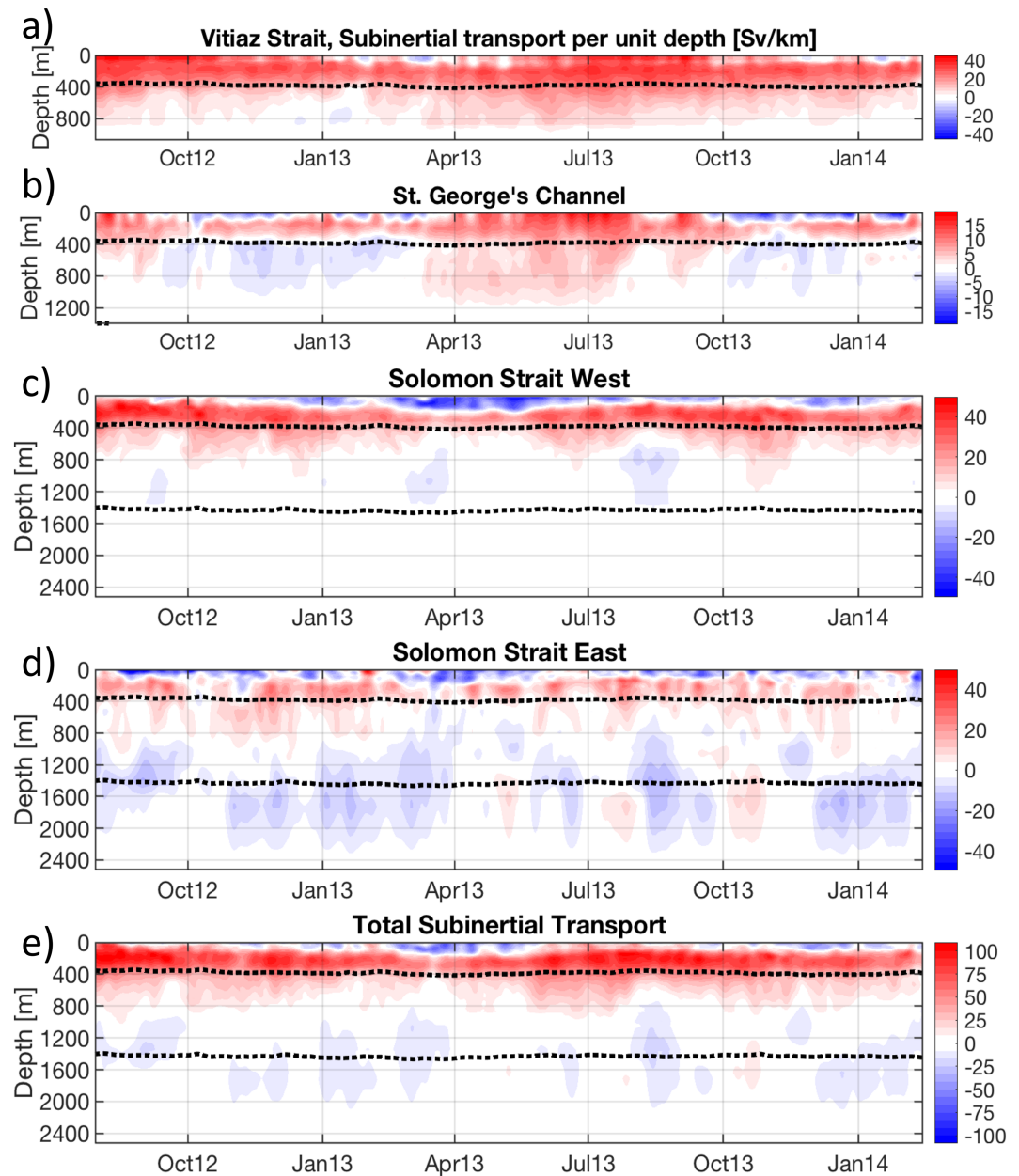
Figure 7. The subinertial transport per unit depth (Sv/km) for (a) Vitiaz Strait, (b) St. George's Channel, (c) Solomon Strait West from New Ireland to Solomon M2, (d) Solomon Strait East from Solomon M2 to the coast of Bougainville Island, and (e) the total transport of from all three channels. Positive values (red) indicate transport exiting the Solomon Sea, while negative values (blue) indicate transport entering the Solomon Sea. The dotted black lines indicate the depth of the σ_0=26.7 and σ_0=27.5 isopycnals. Note the different scales of the color bars for each panel.

thermocline transports (Figure 8a) give rise to enhanced low-pass filtered transport in July–August and reduced transport in January–February, when transport in the top 100 m weakens and reverses.

The observed seasonal strengthening of the surface and thermocline layers in Vitiaz Strait is in agreement with surface drifters (Hristova & Kessler, 2012), SADCP observations (Cravatte et al., 2011; Lindstrom et al., 1990), and prior simulations (Melet et al., 2010a), though no prior observations have resolved sustained reversals of transport in the top 100 m (Figure 7a). Mooring draw down is minimal from November through March, with ADCP coverage up to 50 m below the surface and resolving reversals down to 100-m depth in February, March, and November 2013 and in January 2014. Enhanced surface transports in August through
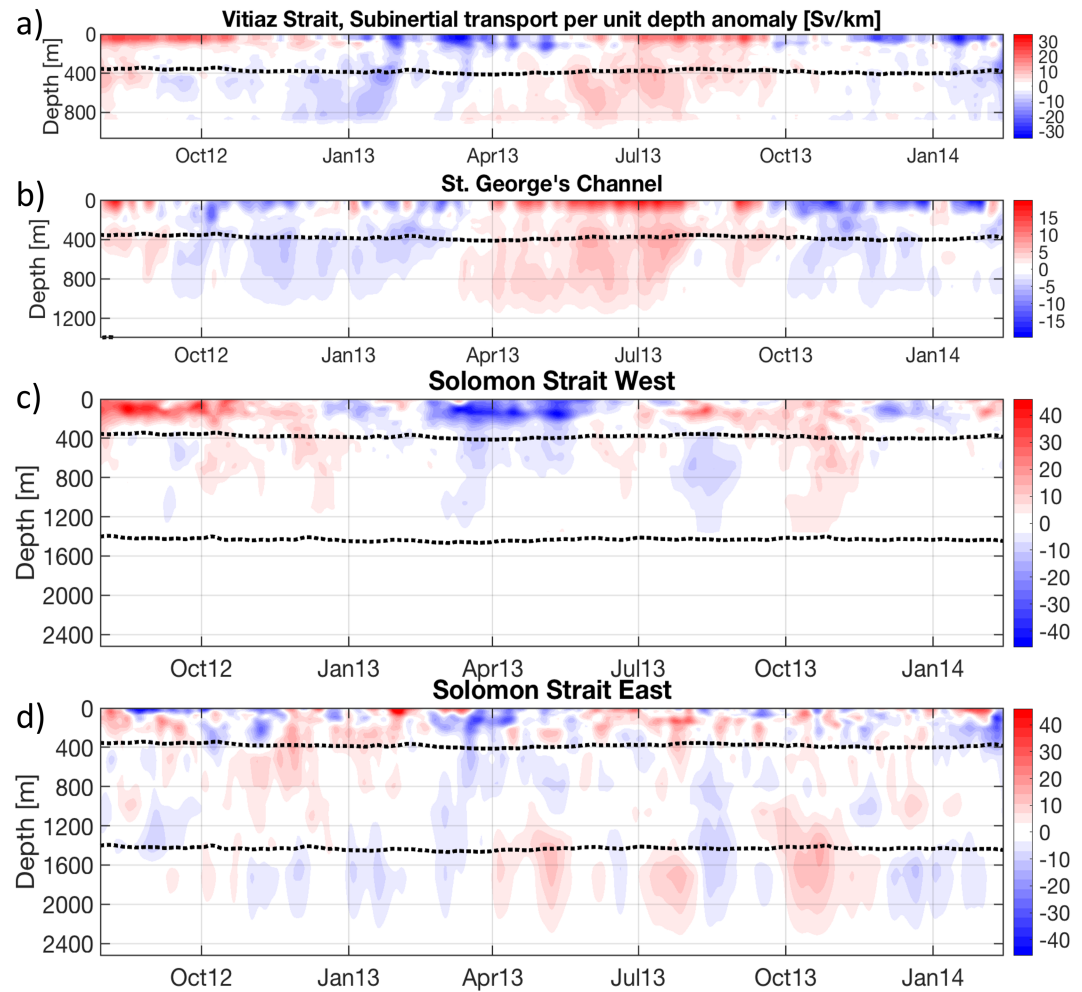
Figure 8. The subinertial transport per unit depth anomaly (Sv/km) for (a) Vitiaz Strait, (b) St. George's Channel, (c) Solomon Strait West from New Ireland to Solomon M2, and (d) Solomon Strait East from Solomon M2 to the coast of Bougainville Island. Positive values (red) indicate transport anomalies exiting the Solomon Sea, while negative values (blue) indicate transport anomalies entering the Solomon Sea. The dotted black lines indicate the mean depths of the σ_0=26.7 and σ_0=27.5 isopycnals. Note the different scales of the color bars for each panel.

October 2012 and in June through August 2013 have large uncertainties due to mooring draw down during those times.

Below the thermocline, seasonal weakening and reversals in December 2012 and January 2013 lead surface reversals by 1–2 months, and intermediate transport is enhanced in June–July 2013 (Figure 8a). While previous observations by Murray et al. (1995) note similar seasonal variability of intermediate transport, deep reversals have not been previously observed in Vitiaz Strait.

Low-pass filtered transport in St. George's Channel remains positive over the deployment period with a mean of 2.3 Sv and standard deviation of 1.8 Sv primarily due the NBCU to transporting water out of the Solomon Sea over 100- to 300-m depth (Figure 6a, dotted red line, and Figure 7b). Low-pass filtered transport is maximum in May–June and minimum in November–December due to transport variations in the top 1,000 m that are nearly in-phase throughout the deployment period (Figures 7b and 8b).

Transport above 100-m depth enters the Solomon Sea from October through February and is estimated to exit the Solomon Sea in April through August (Figure 7b). Mooring draw down is minimal during periods of weak transport (October through February) with ADCP observations extending to 50 m below the surface and resolving sustained periods of surface inflow. Enhanced total channel transport in March to September leads to persistent mooring draw down and reduced ADCP coverage of the upper ocean, resulting in greater

uncertainty of surface transport estimates during these months. Independent SADCP observations suggest that negative transports over the top 100 m may continue into March–May but that surface transports become positive and relatively enhanced in June–August (Cravatte et al., 2011).

Thermocline transport is reduced October through February and enhanced April through August (Figure 8b), consistent with previous simulations of thermocline transport through St. George's Channel (Djath et al., 2014; Melet et al., 2010a). Below the NBCU core, seasonal transport reversals exchange intermediate water masses with the Bismarck Sea. Periods of outflow are stronger and extend deeper into the water column compared to periods of transport into the Solomon Sea, resulting in a net outflow below 400-m depth. Reversal of intermediate currents through St. George's Channel on seasonal time scales has not been previously observed, and prior modeling studies of circulation through the strait have not noted this feature in their results (Coulin et al., 2017; Djath et al., 2014).

Low-pass filtered transport in Solomon Strait exits the Solomon Sea across the western side (6.8 $\pm$ 3.6 Sv) and enters in the eastern part of the Strait (-2.1 ± 1.7 Sv; Figure 6a). Total transport through Solomon Strait West is enhanced in August–October, lagging the seasonal variability observed across the eastern side by 1 month. From August 2012 to October 2012, NICU transport extends up toward the surface (Figure 7c). By December 2012, SEC inflow is observed, deepening and strengthening into April and May 2013, while the NICU weakens, and its vertical extent decreases. In May 2013, the NICU begins to strengthen and extend upward again, while the SEC weakens and shallows until December 2013 when a moderate increase in SEC transport is observed again. This interplay between the vertical extents and strength of the SEC and NICU leads to the observed subsurface maximum in ASV standard deviation east of New Ireland (Figure 4c). Observed thermocline transport anomalies across Solomon Strait West are consistent with simulations by Melet et al. (2010a) and Djath et al. (2014), which also find the NICU to be seasonally enhanced in July–September and reduced in March–April (Figure 8c).

Low-pass filtered total Solomon Sea transport is maximum in July–August and minimum in February, with the largest contribution coming from Vitiaz Strait (Figure 6a). From the surface to 100-m depth, Solomon Strait SEC inflow provides the dominant contribution for both the mean and variability of the total Solomon Sea surface transport (Figure 7e). Total Solomon Sea thermocline transport varies seasonally with Vitiaz Strait and Solomon Strait West contributing comparably. Intermediate transports through Vitiaz Strait and St. George's Channel are nearly in phase with each other and out of phase and counterbalanced by intermediate transport through Solomon Strait West (Figure 7, note the different color bar scales). The resulting total Solomon Sea intermediate transport is thus well described by intermediate transport through Solomon Strait East, which is also the largest observed intermediate transport across the three channels. Solomon Strait East is the sole contributor of deep transport and transport variability in the Solomon Sea.

4.2.2. Intraseasonal Variability

Intraseasonal transport in Vitiaz Strait has 50% less variance than its low-pass filtered transport, and for St. George's Channel, the intraseasonal transport has 30% less variance compared to its low-pass filtered transport. Intraseasonal transports for both channels are also a small and comparable contributions to the total Solomon Sea intraseasonal transport (Figure 6b). At intraseasonal time scales, Solomon Strait transport variability is the largest of the three channels, particularly on the eastern side (Figure 6b, blue lines). In Solomon Strait East, transport anomalies at intraseasonal time scales are evident from the ocean surface to the deepest current meter observation with magnitudes equal to or greater than transport anomalies at seasonal time scales observed in the other channels or section (Figure 8). Intraseasonal total Solomon Sea transport has twice as much variance compared to low-pass filtered total Solomon Sea transport, and Solomon Strait East is responsible for the majority of intraseasonal total transport variability (Figure 6b).

Intraseasonal inflow events between 800- and 1,200-m depth are observed in Solomon Strait West in September 2012 and March and August 2013 when the base of the NICU is shallower and approaches the $\sigma_0 = 26.7$ isopycnal (Figure 7c). Deep transport ($\sigma_0 > 27.5$) generally enters the Solomon Sea across Solomon Strait East along the deep western boundary (Figure 4c), although three outflow events are observed in May, August, and October 2013 (Figure 7d). Simulations by Djath et al. (2014) indicate that this deep inflow varies seasonally, reaching a maximum in December–February and weakening in June–August. Observations do find deep transport to be consistently negative in December to February as predicted, but significant variability is also resolved at intraseasonal time scales even at these depths (Figure 7d).

5. Discussion

5.1. Summary of Results

An average of 22.8±3.5 Sv of total transport from the ocean surface to the base of AAIW (σ_0=27.5) is observed to exit the Solomon Sea through the combination of Vitiaz Strait, St. George's Channel, and Solomon Strait (Table 3). Over half of this transport exits through Vitiaz Strait with 36.2% exiting through Solomon Strait and 9.6% passing through St. George's Channel. A deep transport of −4.6±1.0 Sv is observed to enter the Solomon Sea through Solomon Strait over the deployment period (Figure 4). In the top 100 m, transport enters the Solomon Sea through Solomon Strait and is partially balanced by transport exiting the Solomon Sea through Vitiaz Strait (Figure 5). Total Solomon Sea transport has a subsurface maximum at 200- to 300-m depth, a common feature of all three straits, though Vitiaz Strait and Solomon Strait West transport the dominant contributions. Vitiaz Strait supplies the largest fraction of the total transport, with positive mean transports at all depths, while the large intraseasonal variability of the total Solomon Sea transport is the result of intraseasonal variability in Solomon Strait East (Figures 6 and 7).

5.2. Mean Transport Partitioning

Simulations of circulation in the Solomon Sea previously provided the only estimate of full-depth transport partitioning between Vitiaz Strait, St. George's Channel, and Solomon Strait (Djath et al., 2014; Melet et al., 2011). Over the thermocline, Melet et al. (2010a) estimate a mean transport of 7.2 Sv through Vitiaz Strait and 1.7 Sv through St. George's Channel, in good agreement with observed mean transport over comparable depth and density ranges (Table 3). However, modeled thermocline transport through Solomon Strait (2.5 Sv) is underestimated by a factor of 3 when compared to observed transport in 2012–2014. The simulation also finds a total thermocline transport in the Solomon Sea of 10.8 Sv, significantly less than the observed total thermocline transport (16.2±1.9 Sv; Table 3), which likely contributes to the mismatch in Solomon Strait transport and transport partitioning between the channels. Furthermore, the model described in Melet et al. (2010a) also produces a significant thermocline inflow on the eastern side of Solomon Strait that counters outflowing NICU transport and is not observed over the mooring deployment period. Observations have yet to resolve the interannual variability of transport partitioning or a multiyear mean of full-depth velocity structure in Solomon Strait. At the same time, the model simulates strong interannual variability in transport partitioning at ENSO time scales (Melet et al., 2013), but this interannual partitioning may be dependent on the modeled strait's widths; thus, further observations would be needed to validate interannual partitioning. While those uncertainties remain, it is challenging to diagnose the cause of this observational-model mismatch in Solomon Strait thermocline transport.

Over intermediate densities (corresponding to ∼400- to 1,400-m depth), mooring observations confirm that Vitiaz Strait is an important pathway for water masses exiting the Solomon Sea (Table 3) as previous analysis of hydrographic observations suggest (Germineaud et al., 2016; Qu & Lindstrom, 2002; Tsuchiya, 1991). However, above 650 m, intermediate transport through Solomon Strait is greater than or equal to that through Vitiaz Strait, but Solomon Strait intermediate transport changes sign by 850-m depth (Figure 5a). These results indicate that for upper intermediate waters (400- to 650-m depth), both Vitiaz Strait and Solomon Strait are important equatorward pathways with comparable transport estimates over this depth range. Below 650 m, Vitiaz Strait becomes the dominant equatorward pathway for intermediate waters, while lower intermediate waters enter the Solomon Sea through Solomon Strait and are marked by large temporal variability.

In light of the observed thermocline and intermediate transport partitioning between the Solomon Sea channels, these results indicate that Solomon Strait likely plays a larger role in equatorward water mass transport than previous studies indicated. This especially has implications for previous studies that use Lagrangian particles to track water mass pathways from the Solomon Sea into the equatorial Pacific circulation. While simulations using Lagrangian particles indicate that Vitiaz Strait supplies nearly twice as much transport to the EUC compared to Solomon Strait (Grenier et al., 2011), the mean thermocline and intermediate transports through each channel are not reported. Given the importance of both Vitiaz and Solomon Strait transports for EUC water mass structure, it is necessary to verify that current models accurately partition transport between the two channels. Furthermore, understanding what controls the partitioning of the LLWBCs between the channels remains an open question.

5.3. Vitiaz Strait

The annual cycle of wind stress curl over the South Pacific western subtropical gyre generates a standing Rossby wave that spins the gyre up and down in phase with wind stress curl variability (Kessler & Gourdeau, 2007). Gyre spin up from August to October reduces GPC transport, increases NVJ transport, and results in an anomalously strong NGCC and NBCU (Melet et al., 2010a). This LLWBC strengthening is observed at Vitiaz Strait, where surface and thermocline transports are found to be in phase and correlated (R=0.62 for the surface and R=0.59 for the thermocline) with CCMP wind stress curl over the western subtropical gyre (13–20°S, 150–160°E). While there are prior synoptic observations of surface reversals in Vitiaz Strait (Cravatte et al., 2011; Lindstrom et al., 1990), sustained periods of surface current weakening and reversal have not previously been observed (Figure 7a).

Near-surface velocities in Vitiaz Strait are also found to be in phase, aligned, and well correlated with local CCMP winds (R=0.71), including over the sustained periods of surface transport reversals, when ADCP coverage extends up to 50-m depth. Since Vitiaz Strait is narrow, surface flow is constrained by topography, and the Coriolis force is relatively weak at this latitude, it is likely that surface flow is accelerated by and aligned with wind stress.

Seasonal-scale intermediate transport anomalies are observed to lead thermocline and surface transport anomalies by 2–3 months in Vitiaz Strait, with anomalies propagating upward starting in October 2012 and April 2013. Such behavior may indicate that transport through Vitiaz Strait is seasonally modulated by downward propagating planetary waves, which would produce upward propagating anomalies. The propagation of planetary waves through the Solomon Sea and Vitiaz Strait is likely complicated by the area's topography. While further investigation into this mechanism is beyond the scope of this paper, the role of such waves in modulating Solomon Sea LLWBC transports over a range of time scales merits future study.

5.4. Solomon Strait

Seasonal variability of the SEC is driven by the annual propagation of off-equatorial Rossby waves that modulate the meridional location of the SEC and thus where the current impinges upon the eastern boundary of the Solomon Sea (Melet et al., 2010b). Simulations by Melet et al. (2010a) also indicate a westward propagation of the annual transport anomalies across Solomon Strait with anomalies on the western side lagging those on the eastern side by approximately 1 month and maximum seasonal transport on the western side of the strait in October–November. In addition, the modeled seasonal cycle of SEC thermocline transport on the eastern side of Solomon Strait varies zonally, aligned with the channel cross section, while the seasonal cycle on the western side has the largest variability in the direction parallel to the coast of New Ireland, nearly orthogonal to the western cross section (Melet et al., 2010a, their figure 6).

As such, it is not surprising that surface and thermocline transports across Solomon Strait West are well correlated (R=−0.75 for the surface layer and R=−0.84 for the thermocline) and in phase opposition with sea level anomalies (SLA) outside Solomon Strait where the annual Rossby wave is observed to reach the Solomon Sea (SLA averaged over 4–6°S, 155–158°E, not shown). Positive SLA anomalies in this region indicate the presence of a downwelling Rossby wave east of Solomon Strait that enhances westward SEC transport equatorward of the Rossby wave crest and thus transport into the Solomon Sea (Melet et al., 2010a; 2010b). These westward SEC anomalies manifest as negative transport anomalies across Solomon Strait West in both the surface and thermocline layers. The low-pass filtered transport out of Solomon Strait West is also maximum in October and lags seasonal time scale variability of transport through Solomon Strait East by 1 month, in agreement with predictions.

Thermocline transport across Solomon Strait East is only weakly correlated (R=−0.39) with SLA outside of Solomon Strait, and surface transports across Solomon Strait East are not strongly correlated with the annual Rossby wave SLA ($|R|$<0.2 for time lags/leads ≤100 days). The zonal orientation of the annual variability of transport on the eastern side of Solomon Strait likely contributes to the weak correlation between upper ocean transport and SLA associated with the annual Rossby wave. Additionally, given that there is 10 times more variance at intraseasonal time scales compared to seasonal time scales in Solomon Strait East, a weak correlation with seasonal scale forcing is not surprising. Other dynamical features, such as mesoscale eddies, may have a stronger influence on transport variability across Solomon Strait East, potentially responsible for the enhanced variance observed at intraseasonal time scales. Both observations (Gourdeau et al., 2017; Melet

et al., 2010b) and simulations (Djath et al., 2014; Hristova et al., 2014; Srinivasan et al., 2017) indicate that mesoscale and submesoscale eddies are enhanced at Solomon Strait and are a likely source of intraseasonal transport variability.

Transport anomalies are generally coherent over intermediate and deep isopycnals across Solomon Strait East (Figures 7d and 8d). Alternating westward and eastward zonal jets that are coherent vertically from 600- to 1,500-m depth at basin scale are observed to originate or recirculate at the eastern side of the Solomon Sea near Solomon Strait (Cravatte et al., 2012, 2017). The connections between the Solomon Sea and these basin-scale zonal currents are not well understood but could be of importance for the redistribution of water masses at intermediate depths. Prior observations indicate seasonal variability of the depths of these zonal jets due to the downward propagation of annual Rossby waves (Kessler & McCreary, 1993; Marin et al., 2010). Maximum westward anomalies at the latitude and longitude of Solomon Strait are observed in December–May with eastward anomalies in June–November. Westward anomalies are expected to translate to negative transport anomalies through Solomon Strait, but this is not what is observed in Figure 7. It is probable that interactions with topography near Solomon Strait complicate this seasonal variability. While our observations do not offer conclusive evidence that the vertically coherent variabilities over intermediate and deep layers in Solomon Strait are linked to the annual zonal jet anomalies outside of the Sea, understanding the connections between the basin wide deep zonal jets and the Solomon Sea waters merits further investigation.

5.5. St. George's Channel

Previous modeling work suggests that 61% of surface water transport through St. George's Channel can be traced back to Solomon Strait (Melet et al., 2011), suggesting that surface transport variability in Solomon Strait has a direct connection to St. George's Channel. Surface transport through St. George's Channel is moderately correlated ($R=-0.51$) with surface transport through Solomon Strait West, with periods of anomalous SEC transport into the Solomon Sea through Solomon Strait West leading enhanced surface transport out through St. George's Strait by 45 days (Figures 8b and 8c). While local winds are also expected to have an influence on surface currents, surface currents in St. George's Channel are not well correlated with local CCMP winds ($R=0.27$). The lack of clear relationship could stem from the large uncertainties in surface current direction and magnitude during the months of March to September and/or the quality of the CCMP surface winds in the very narrow St George's Channel.

Simulations indicate that 90% of thermocline transport in St. George's Channel is supplied by the NBCU (Melet et al., 2011). Thus, the strength of thermocline transport through St. George's Channel is expected to depend upon the strength of the NBCU and the partitioning of the NBCU between St. George's Channel and Solomon Strait. Model results indicate that NBCU transport varies seasonally and is maximum in September. Thermocline transport in St. George's Channel is maximum in May–June, 3–4 months before NBCU thermocline transport is predicted to be maximum (Figures 7b and 8b). However, the sum of thermocline transport in St. George's Channel and Solomon Strait West varies seasonally and in phase with modeled NBCU transport variability, suggesting that NBCU partitioning also varies seasonally. What determines the partitioning of the NBCU between the two channels remains an open question.

While intermediate transport through St. George's Channel is small, the seasonal exchange of water masses between the Solomon Sea and Bismarck Sea may be of importance, particularly if deep-sea mining operations are planned for the Bismarck Sea. Material transport associated with mining plumes was recently modeled by Coulin et al. (2017) for the region and specifically in St. George's Channel. That and previous modeling studies have not noted seasonal reserving of intermediate transports in their results (Djath et al., 2014; Melet et al., 2011; Srinivasan et al., 2017). The observed sustained reversals will influence the transport of materials which operational forecasts that are needed for assessing the impacts of mining operations in the region may not resolve at present.

6. Final Remarks

Accurately estimating the transport and partitioning of South Pacific LLWBC transport into the Equatorial Pacific is necessary to correctly simulate EUC water mass properties and variability. These observations have, for the first time, simultaneously resolved thermocline-to-sill-depth transport, variability, and

channel partitioning in the Solomon Sea over an 18-month deployment. Because transport estimates are sensitive to cross-passage extrapolation schemes, an intercomparison of the moored velocity observations and modeled profiles of velocity in the Solomon Sea straits might productively help constrain the contributions of Vitiaz Strait and Solomon Strait waters to the EUC. These results suggest that the contribution of transport from Solomon Strait to the EUC may be underestimated in regional and global models at present. This has implications for understanding the nutrient sources of equatorial Pacific primary productivity as iron concentrations are strongly tied to transit times and parcels traveling from Solomon Strait reach the EUC more quickly than those exiting from Vitiaz Strait (Grenier et al., 2011; Qin et al., 2016).

Significant uncertainty still remains concerning the variability of surface currents in the Solomon Sea channels. In Vitiaz Strait and St. George's Channel, the strong currents and highly trafficked channels make traditional mooring observations challenging and limit observations of temperature and salinity in the upper part of the water column. In Solomon Strait, surface geostrophic velocities from satellite products have limited capabilities due to signal contamination by nearby land, limiting reliable estimates to the middle of the strait. Novel observing techniques will likely be needed if future studies wish to better resolve upper ocean currents and water properties. High-frequency radar observations could potentially be utilized to measure surface currents, as these platforms have the capability to resolve hourly currents at kilometer-scale horizontal resolution across the straits (Paduan & Washburn, 2013). It should be noted, however, that such radar systems may present operational challenges due to power consumption, logistical operations, and maintenance requirements.

The LLWBCs of the Solomon Sea have been highlighted by the Tropical Pacific Observing System 2020 project as a key component of tropical circulation that requires sustained monitoring (Cravatte et al., 2016; Smith et al., 2019). To successfully monitor transport through the Solomon Sea, planned observing systems will need to be designed such that the strong intraseasonal variability observed in Solomon Strait is not aliased onto annual and interannual time series. Long-term mooring deployments in Solomon Strait may be a potential solution given the observed large intraseasonal variability in the strait, relatively high data return, and minimal mooring draw down compared to Vitiaz Strait and St. George's Channel.

During the mooring deployment period, repeated glider transects (Davis et al., 2012; Kessler et al., 2019) and an array of bottom pressure sensors with dynamic height moorings (Anutaliya et al., 2019) were deployed in the southern section of the Solomon Sea, independently monitoring transport through the southern opening. The glider observations are the longest source of continuous transport observations in the Solomon Sea, providing quality estimates of seasonal and interannual transport, but their sampling scheme aliases intraseasonal transport variability. The array of bottom pressure sensors with dynamic height moorings resolves intraseasonal transport variability but does not resolve the vertical structure of transport in the Solomon Sea. All three observing systems have different strengths and would benefit from an intercomparison of transport estimates during the overlapping deployment periods. The results from such an intercomparison would be very valuable for designing a long-term monitoring system for the Solomon Sea LLWBCs as recommended for Tropical Pacific Observing System 2020.

Finally, while superinertial motions are beyond the scope of this paper, these mooring observations fully resolved up to diurnal and semidiurnal frequencies in all three channels over much of the water column. Velocity variance at these frequencies is significant compared to that at subinertial frequencies. Such processes are generally important for water mass modification and are likely influenced by the subinertial processes described within this paper.

Appendix A: Extended Discussion of Data and Methods

A.1 Estimated Salinity at 1,700-m Depth on Mooring Solomon M2

One goal of the moorings deployed in Solomon Strait was to measure geostrophic transport using arrays of CTDs deployed across the three moorings. A significant loss for the Solomon Strait moorings was the failure of the deepest CTD sensor at 1,700-m depth on the central mooring, Solomon M2a. As the next deepest conductivity sensor on Solomon M2a was located at 700-m depth, this loss would limit the geostrophic transport estimate to above 700-m depth. In an attempt to mitigate this loss, the temperature and pressure record from a sensor deployed at 1,700-m depth on Solomon M2b and nine shipboard CTD profiles from the Pandora and
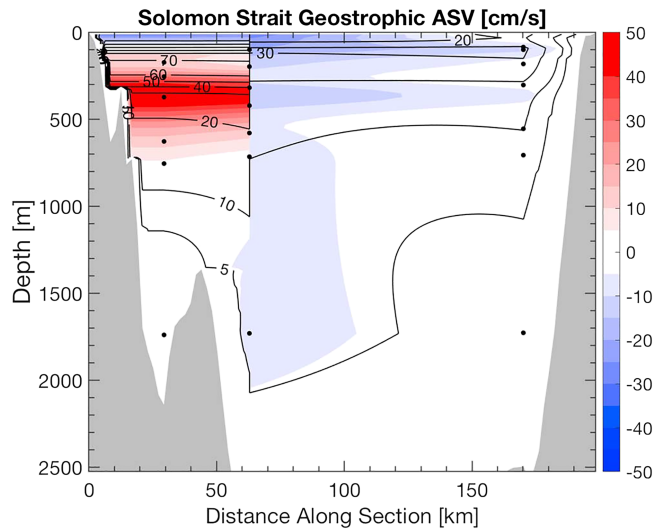
Figure A1. The mean (red-blue color map) and standard deviation (black contours) of the along-strait velocity (ASV; cm/s) for Solomon Strait estimated using geostrophy. Statistics were calculated over the deployment period, and the vertical limits are the ocean surface to each channel's respective sill depth. Mean ASV sections are contoured at 5 cm/s increments, and red indicates transport exiting the Solomon Sea, while blue indicates transport entering. The standard deviation of the along-strait velocity is contoured in 10 cm/s intervals with an additional 5 cm/s contour. Deployment-mean locations of all density observations are indicated with black dots for the directly observed velocity sections. Note the discontinuity across Solomon Strait is due to the discontinuous transect line used for the channel cross section (Figure 1b).

MoorSPICE cruises taken at the mooring location are used to estimate the missing salinity record. Over the range of temperatures observed by a thermistor at 1,700 m on Solomon M2b (3–2.3 °C), a tight linear relationship between temperature and salinity is found from the shipboard CTD profiles ($R=-0.99$). Thus, salinity for the temperature sensor moored at 1,700 m is estimated based on the linear relationship determined from the CTD profiles. To test the potential error associated with this method, a similar analysis is performed for the CTD sensors at 1,700-m depth on moorings Solomon M1 and M3. CTD casts at the locations of mooring Solomon M1 and M3 also are found to have tight linear relationships between temperature and salinity, with $R=-0.99$ for both moorings, over the temperature ranges observed by each CTD sensor. Salinity time series are estimated from the linear relationships for both CTD sensors and compared with the sensor's observed salinity. A root-mean-square difference between the observed and estimated salinity of 0.0017 PSU for Solomon M1 and 0.0021 PSU for Solomon M3 is found.

A.2 Geostrophic Velocity in Solomon Strait

Using the maximum mean ASV (60 cm/s) and channel width (185 km), which limits the lateral scale of flow, Solomon Strait is found to have a Rossby number less than unity ($Ro=0.3$); thus, we expect that even for the fastest flows, the effect of planetary rotation is important within Solomon Strait. Given the lateral scale over which transport needs to be estimated, one might expect that sufficiently high-resolution profiles of density and velocity on either side of the channel would give an accurate geostrophic estimate of transport through the strait when compared to a linear interpolation of the velocity profiles.

However, it is not certain that the interpolated velocity profiles would give an accurate approximation of the geostrophic transport in this wide strait where ageostrophic flows might also contribute. Under this hypothesis, we chose to use the geostrophic approximation to estimate transport in the channel.

On average, the shallowest density observations are at 170-, 90-, and 80-m depth for Solomon M1, M2, and M3, respectively, and extend down to 1,700-m depth for all three mooring locations (Figure A1, black dots indicate mean location of density observations). Discrete density observations from CTD sensors are linearly interpolated onto a regular vertical grid with 20-m spacing. Gridded density (ρ) is used to estimate vertical shear using the Thermal Wind equations:

$$-f\frac{\partial v_{\mathrm{g}}}{\partial z} = g\frac{\partial \rho}{\partial x}, \quad f\frac{\partial u_{\mathrm{g}}}{\partial z} = g\frac{\partial \rho}{\partial y}, \tag{A1}$$

where u_{g} and v_{g} are geostrophic velocity, f is the Coriolis frequency, and g is gravitational acceleration. As geostrophy can only estimate the component of the flow normal to the line between profiles of density, geostrophic shear is estimated separately for Solomon Strait West and East. For Solomon Strait West (between Solomon M1 and M2), geostrophic shear in the along-strait direction is estimated from 170 m down to 1,350-m depth, below which a sea mount impedes the calculation. At Solomon M1 and M2, the observed ASV at 1,350 m is used to integrate the shear vertically upward, and below 1,350 m, the directly observed ASV is used from 1,350 m down to 1,700-m depth. For Solomon Strait East, (between M2 and M3), the along-strait component of geostrophic shear is estimated from 90 m down to 1,700-m depth. At each mooring along Solomon Strait East, shear is integrated vertically and referenced to the observed ASV at 1,700-m depth.

Because geostrophy estimates vertical shear from the lateral density gradient at a particular depth, it is optimal to have concurrent density observations at the same depth. While the moorings were designed to measure density at many of the same depths across Solomon Strait, mooring draw down, which varies in time and between moorings, results in sensors measuring significantly different depths across the three
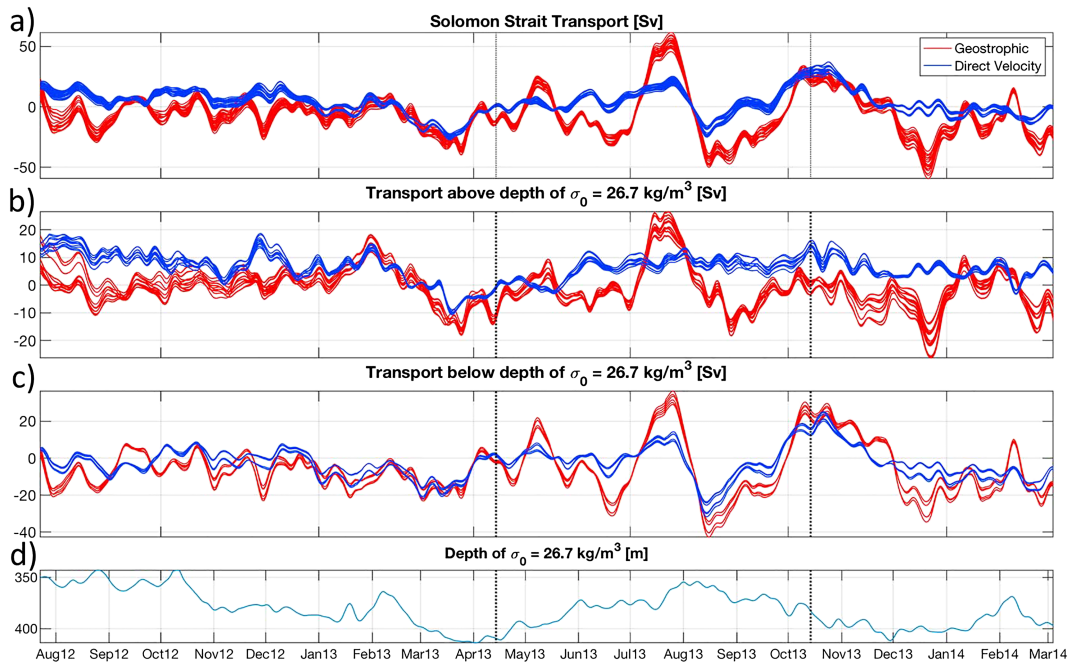
Figure A2. Transport time series at Solomon Strait from (a) the surface to sill depth, (b) the surface the depth of the σ_0=26.7 isopycnal, and (c) the depth of the σ_0=26.7 isopycnal to the sill depth for all model combinations using geostrophy (red lines) and in situ velocity (blue lines) to estimate transport. (d) Time series of mean σ_0=26.7 isopycnal depth in Solomon Strait. The time of instrument failures on mooring Solomon M2 are demarcated by the dotted black lines in all panels.

moorings at any given time, though increased vertical resolution of sensors helps to mitigate this problem. Nonetheless, for portions of the water column where the vertical structure of density is not well approximated by linear interpolation, namely, above the thermocline, the vertical interpolation process will result in biased estimates of the density gradients across Solomon Strait. Additionally, the failure of two CTDs at 300- and 550-m depth at mooring Solomon M2 further degrades the quality of the geostrophic estimate over the latter half of the transport time series.

The same vertical and cross-passage extrapolation schemes described in sections 3.2 and 3.3 are used to generate gridded cross sections of geostrophic ASV. For the Satellite Inferred method, the shallowest geostrophic ASV is linearly interpolated to the satellite surface geostrophic estimate, and the Ekman profile is added to the profile of geostrophic ASV. The mean ASV cross section over the deployment period estimated from geostrophy for Solomon Strait using the Satellite Inferred, Linear to Bottom, and Boundary Intensification schemes is shown in Figure A1 for reference.

A.3 Transport From Geostrophy and Direct Observations of Velocity in Solomon Strait

The mean cross-sectional structure of ASV from the geostrophic estimate agrees well with in situ velocity observations on the western side of the strait below 200-m depth and below 1,000-m depth on the eastern side. Above 1,000-m depth, geostrophic transport is estimated to flow in the opposite direction through Solomon Strait East compared to in situ velocity observations. Only the Satellite Inferred surface scheme replicates the shallow inflow above 100-m depth that is also observed in the mean SADCP cross section, as the geostrophic estimate cannot, on average, resolve the top 170 m of the water column at Solomon Strait West.

Total transport time series estimated using geostrophy and in situ velocity observations in Solomon Strait are compared in Figure A2a, with individual lines representing each permutation of the various extrapolation methods. The method-averaged Solomon Strait transports (σ_0<26.7) estimated from geostrophy and in situ velocity observations are well correlated from July 2012 until April 2013 (R=0.59, p value =0.00, degrees of freedom = 265) but are weakly (R=0.12) and less statistically significantly correlated (p value =0.03, degrees of freedom = 323) after the loss of the CTD at 550-m depth in April 2013 (Figure A2b). Degrees of

freedom are equal to the number points from the time series used to calculate correlation less one. Below the base of the thermocline, transports remain well correlated over the entire deployment period (R=0.81, p value =0.00, degrees of freedom = 589), but the range of transport from the geostrophic estimate increases significantly compared to the transport estimate from direct observations after April 2013 (Figure A2c). The reasonable agreement in transport variability prior to the loss of CTD coverage on Solomon M2a suggests that transport estimated from in situ velocity observations may be a reasonable estimate of mesoscale transport.

A.4 Sensitivity of Transport to Vertical Extrapolation

To investigate the consistency of the vertical extrapolation schemes compared to previous observations, historical (Cravatte et al., 2011) and recent (Ganachaud et al., 2017; Germineaud et al., 2016) SADCP profiles located within 20 km of the above-defined channel cross sections (Figure 1b) were projected onto the along-strait direction and averaged across each channel to produce mean ASV cross sections (Figures 2 and 3, black contours). It should be noted that profiles at these locations are predominately from the months of February to July, with the largest data contribution coming from July 2012 and March 2014; thus, seasonal bias likely contributes to the SADCP mean ASV cross-channel structure. These mean SADCP sections are compared to examples of ASV cross sections produced using the different vertical schemes for each channel (Figures 2 and 3, red-blue filled contours).

In Solomon Strait, Constant Shear and Satellite Inferred surface models both replicate the shallow reversal of the flow near New Ireland and produce surprisingly similar estimates of the mean ASV cross section, with deployment-mean transport differing by only 0.9% (Figures 2f and 2g and Table 4). An additional Satellite Inferred surface model was tested for Solomon Strait using Eulerian surface velocities (Ekman + Geostrophic) from the GlobCurrent analysis (http://globcurrent.ifremer.fr/; Rio et al., 2014). Solomon Strait transport was insensitive to the choice of GlobCurrent, with transport changing by <3% compared to the previously described Satellite Inferred method.

The mean SADCP section in Solomon Strait does indicate that the western inflow has a subsurface maximum rather than being surface intensified as is suggested by the Satellite Inferred schemes (Figure 2). While this shallow inflow is above the mean depth of the shallowest ADCP bin (70-m depth) of Solomon M1, the upward-looking ADCP at M1 does resolve a pronounced inflow from the surface extending down to 200 m in February–June 2013 when mooring draw down is minimal and coverage extends up to 10- to 30-m depth. As most SADCP profiles are also from these months, it is possible that this is a seasonal feature over represented in the SADCP data and not representative of mean vertical structure. There remains uncertainty for both the SADCP and moored ASV mean sections in the top 70 m near New Ireland during the months of September–December.

In Vitiaz Strait, the Slab to Surface vertical extrapolation scheme is most representative of the mean SADCP transect (Figures 3a and 3b) and consistent with observations of the mean ASV cross section by Cravatte et al. (2011). In addition, transport through Vitiaz Strait is relatively insensitive to the chosen surface model with the deployment-mean total channel transport decreasing by 3.7% when the Constant Shear surface model is used rather than the Slab model (Table 4).

For St. George's Channel, the Constant Shear model is a better approximation of the mean SADCP ASV cross section, which is strongly sheared above 200 m and reverses direction from inflow to outflow below 100-m depth (Figures 3c and 3d). Mean ASV cross sections in St. George's Channel from Cravatte et al. (2011) also indicate that the current is sheared above 200 m, approaching zero or potentially reversing above 50- to 100-m depth. Since, on average, the top 100 m of the water column in St. George's Channel was unresolved, transport through St. George's Channel is more sensitive to the surface model with the deployment-mean total channel transport decreasing by 9.6% when the Constant Shear model is used compared to the Slab to Surface model (Table 4).

In Solomon Strait, transport is sensitive to the bottom extrapolation scheme. Relatively strong flow (mean ASV of 8 cm/s) is observed entering the Solomon Sea at 1,700-m depth at Solomon M2 and is interpolated across a vertical extent of 825 m to the channel's sill depth (2,525-m depth). Deployment-mean transport increases by 43.2% when Linear to Bottom is used rather than Slab to Bottom. No published observations

exist to support a choice for the most appropriate near-bottom extrapolation model for Solomon Strait; however, the linear interpolation to zero at bottom is the more conservative choice.

The transport through Vitiaz Strait is not sensitive to the bottom model (Table 4), as the ADCP observations extend nearly to the sill depth for the entire deployment period (Figures 4a and 4b). The estimated transport is essentially insensitive to the bottom model in St. George's Channel as well, with only a 0.6% decrease in deployment-mean transport when the Linear to Bottom model is employed rather than the Slab to Bottom.

A.5 Sensitivity of Transport to Cross-Passage Extrapolation

Deployment-mean transport is sensitive to the lateral interpolation model for all three channels (Table 4). Cross-channel ASV structure similar to the Linear and Nearest Across Channel methods are found in synoptic observations of Vitiaz Strait and St. George's Channel, indicating temporally varying velocity structures. Furthermore, the Linear Across Channel scheme provides a conservative, lower bound for the mean transport, while the Nearest Across Channel is likely an upper bound for all three channels. Modeled and observed ASV cross sections are found to have enhanced velocities along the western boundary in Vitiaz and Solomon Strait and along the eastern boundary in St. George's Channel (Cravatte et al., 2011; Djath et al., 2014; Germineaud et al., 2016; Lindstrom et al., 1990). This cross-channel structure is best approximated by the Boundary Intensification method.

Solomon Strait mean transport increases by 41.6% when the Nearest Across Channel method is used compared to Linear Across Channel (Table 4). The Boundary Intensification model similarly increases mean transport by 55.5% compared to the Linear method. These sensitivity estimates indicate that Solomon Strait mean transport is most sensitive to extrapolation of ASV at Solomon M1 to the western boundary. Observations by Cravatte et al. (2011) and the mean SADCP ASV along the mooring transect indicate that NICU ASV extends from the current core to the western boundary (Figure 2). In both the moored and SADCP mean ASV cross sections, the NICU also extends almost 100 km east from the coast of New Ireland (Figure 2).

In Vitiaz Strait, mean transport increases by 63.5% using the Boundary Intensification model compared to Linear Across Channel and nearly doubles when the Nearest scheme is used rather than Linear (Table 4). Mean SADCP cross sections of ASV by Cravatte et al. (2011) indicate that ASV is enhanced on the western side of the channel with ASV decreasing to 50 cm/s on the eastern side of the channel. Reasonable agreement in mean ASV cross-channel current structure is found between the Boundary Intensification scheme and mean SADCP channel cross section for Vitiaz Strait (Figure 3). Synoptic observations by Lindstrom et al. (1990) find western boundary intensification of the NGCU in Vitiaz Strait in January 1986 but also suggest variability in the ASV current structure as the NGCU had a double core in the center of the channel in July 1985. However, both synoptic cross sections have weaker ASV on the eastern side of Vitiaz Strait. Transects by Germineaud et al. (2016) indicate slight western intensification of ASV in Vitiaz Strait with ASV of 80–100 cm/s extending to both sidewalls. These observations suggest that the Linear model likely underestimates transport through Vitiaz Strait while the Boundary Intensification or Nearest Across Channel models provide more realistic estimates.

Mean transport through St. George's Channel increases by 24.2% or 42.4% when the Boundary Intensification or Nearest Across Channel schemes, respectively, are used to estimate cross-channel ASV structure rather than the Linear model. Eastern boundary intensification is observed for the mean ASV cross section by Cravatte et al. (2016) and in synoptic surveys by Lindstrom et al. (1990). While the Boundary Intensification scheme produces an estimate of mean ASV with cross-channel current structure that is similar to prior observations, there are not sufficient SADCP profiles near the mooring transect for a conclusive comparison with the interpolation schemes (Figures 3c and 3d).

References

Alberty, M. S., Germineaud, C., Sprintall, J., Ganachaud, A., & Cravatte, S. (2017). SPICE mooring data report: Description and quality control. UC San Diego: Scripps Institution of Oceanography. Retrieved from https://escholarship.org/uc/item/6xd149s8

Alberty, M., Sprintall, J., MacKinnon, J., Germineaud, C., Cravatte, S., & Ganachaud, A. (2019). Data from: Moored observations of transport in the Solomon Sea, *Solomon Sea SPICE mooring data*: UC San Diego Library Digital Collections. https://doi.org/10.6075/J0639N12

Anutaliya, A., Send, U., Sprintall, J., McClean, J. L., Lankhorst, M., & Koelling, J. (2019). Mooring and seafloor pressure end-point measurements at the southern entrance of the Solomon Sea: Subseasonal to interannual flow variability. *Journal of Geophysical Research: Oceans*, *124*, 5085–5104. https://doi.org/10.1029/2019JC015157

Atlas, R., Hoffman, R. N., Ardizzone, J., Leidner, S. M., Jusem, J. C., Smith, D. K., & Gombos, D. (2011). A cross-calibrated, multiplatform ocean surface wind velocity product for meteorological and oceanographic applications. *Bulletin of the American Meteorological Society*, *92*(2), 157–174.

Butt, J., & Lindstrom, E. (1994). Currents off the east coast of New Ireland, Papua New Guinea, and their relevance to regional undercurrents in the western equatorial Pacific Ocean. *Journal of Geophysical Research*, *99*(C6), 12,503–12,514.

Coulin, J., Haley, P., Jana, S., Kulkarni, C. S., Lermusiaux, P. F., & Peacock, T. (2017). Environmental ocean and plume modeling for deep sea mining in the Bismarck Sea, *OCEANS 2017 - Anchorage* (pp. 1–10): IEEE.

Cravatte, S., Ganachaud, A., Duong, Q.-P., Kessler, W. S., Eldin, G., & Dutrieux, P. (2011). Observed circulation in the Solomon Sea from SADCP data. *Progress in Oceanography*, *88*(1), 116–130.

Cravatte, S., Ganachaud, A., Sprintall, J., Alberty, M., & Germineaud, C. (2019). Solomon Sea SPICE Mooring Data 2012–2014, *Solomon Sea SPICE mooring data*: UC San Diego Library Digital Collections. https://doi.org/10.6075/J02B8WBS

Cravatte, S., Ganachaud, A., Sprintall, J., Alberty, M., Germineaud, C., Brachet, C., et al. (2019). Solomon Sea SPICE mooring data. UC San Diego Library Digital Collections. https://doi.org/10.6075/J09W0CS2

Cravatte, S., Kessler, W. S., & Marin, F. (2012). Intermediate zonal jets in the tropical Pacific Ocean observed by Argo floats. *Journal of Physical Oceanography*, *42*(9), 1475–1485.

Cravatte, S., Kessler, W., Smith, N., Wijffels, S., & Contributing Authors (2016). First Report of TPOS 2020(*GOOS-215*).

Cravatte, S., Kestenare, E., Marin, F., Dutrieux, P., & Firing, E. (2017). Subthermocline and intermediate zonal currents in the tropical Pacific Ocean: Paths and vertical structure. *Journal of Physical Oceanography*, *47*(9), 2305–2324.

Davis, R. E., Kessler, W. S., & Sherman, J. T. (2012). Gliders measure western boundary current transport from the South Pacific to the Equator*. *Journal of Physical Oceanography*, *42*(11), 2001–2013.

Djath, B., Verron, J., Melet, A., Gourdeau, L., Barnier, B., & Molines, J.-M. (2014). Multiscale dynamical analysis of a high-resolution numerical model simulation of the Solomon Sea circulation. *Journal of Geophysical Research: Oceans*, *119*, 6286–6304. https://doi.org/10.1002/2013JC009695

Fine, R. A., Lukas, R., Bingham, F. M., Warner, M. J., & Gammon, R. H. (1994). The western equatorial Pacific: A water mass crossroads. *Journal of Geophysical Research*, *99*(C12), 25063–25080.

Ganachaud, A., Cravatte, S., Melet, A., Schiller, A., Holbrook, N., Sloyan, B., et al. (2014). The Southwest Pacific Ocean circulation and climate experiment (SPICE). *Journal of Geophysical Research: Oceans*, *119*, 7660–7686. https://doi.org/10.1002/2013JC009678

Ganachaud, A., Cravatte, S., Sprintall, J., Germineaud, C., Alberty, M., Jeandel, C., et al. (2017). The Solomon Sea: Its circulation, chemistry, geochemistry and biology explored during two oceanographic cruises. *Elementa: Science of the Anthropocene*, *5*, 33.

Gasparin, F., Ganachaud, A., Maes, C., Marin, F., & Eldin, G. (2012). Oceanic transports through the Solomon Sea: The bend of the New Guinea Coastal Undercurrent. *Geophysical Research Letters*, *39*, L15608. https://doi.org/10.1029/2012GL052575

Germineaud, C., Ganachaud, A., Sprintall, J., Cravatte, S., Eldin, G., Alberty, M. S., & Privat, E.(2016). Pathways and water mass properties of the thermocline and intermediate waters in the Solomon Sea. *Journal of Physical Oceanography*, *46*(10), 3031–3049.

Gourdeau, L., Verron, J., Chaigneau, A., Cravatte, S., & Kessler, W. (2017). Complementary use of glider data, altimetry, and model for exploring mesoscale eddies in the tropical Pacific Solomon Sea. *Journal of Geophysical Research: Oceans*, *122*, 9209–9229. https://doi.org/10.1002/2017JC013116

Grenier, M., Cravatte, S., Blanke, B., Menkes, C., Koch-Larrouy, A., Durand, F., et al. (2011). From the western boundary currents to the Pacific equatorial undercurrent: Modeled pathways and water mass evolutions. *Journal of Geophysical Research*, *116*, C12044. https://doi.org/10.1029/2011JC007477

Grenier, M., Jeandel, C., & Cravatte, S. (2014). From the subtropics to the equator in the Southwest Pacific: Continental material fluxes quantified using neodymium data along modeled thermocline water pathways. *Journal of Geophysical Research: Oceans*, *119*, 3948–3966. https://doi.org/10.1002/2013JC009670

Hristova, H. G., & Kessler, W. S. (2012). Surface circulation in the Solomon Sea derived from Lagrangian drifter observations*. *Journal of Physical Oceanography*, *42*(3), 448–458.

Hristova, H. G., Kessler, W. S., McWilliams, J. C., & Molemaker, M. J. (2014). Mesoscale variability and its seasonality in the Solomon and Coral Seas. *Journal of Geophysical Research: Oceans*, *119*, 4669–4687. https://doi.org/10.1002/2013JC009741

Hu, D., Cui, M., Qu, T., & Li, Y. (1991). A subsurface northward current off Mindanao identified by dynamic calculation. *Elsevier oceanography series*, *54*, 359–365.

Kawabe, M., Kashino, Y., & Kuroda, Y. (2008). Variability and linkages of New Guinea Coastal Undercurrent and lower equatorial intermediate current. *Journal of Physical Oceanography*, *38*(8), 1780–1793.

Kessler, W. S., & Cravatte, S. (2013). Mean circulation of the Coral Sea. *Journal of Geophysical Research: Oceans*, *118*, 6385–6410. https://doi.org/10.1002/2013JC009117

Kessler, W. S., & Gourdeau, L. (2007). The annual cycle of circulation of the southwest subtropical Pacific, analyzed in an ocean GCM. *Journal of Physical Oceanography*, *37*(6), 1610–1627.

Kessler, W. S., Hristova, H. G., & Davis, R. E. (2019). Equatorward western boundary transport from the South Pacific: Glider observations, dynamics and consequences. *Progress in Oceanography*, *175*, 208–225.

Kessler, W. S., & McCreary, J. P. (1993). The annual wind-driven rossby wave in the subthermocline equatorial Pacific. *Journal of Physical Oceanography*, *23*(6), 1192–1207.

Labatut, M., Lacan, F., Pradoux, C., Chmeleff, J., Radic, A., Murray, J. W., et al. (2014). Iron sources and dissolved-particulate interactions in the seawater of the Western Equatorial Pacific, iron isotope perspectives. *Global Biogeochemical Cycles*, *28*, 1044–1065.

Lindstrom, E., Butt, J., Lukas, R., & Godfrey, S. (1990). The flow through Vitiaz Strait and St. George's Channel, Papua New Guinea, *The physical oceanography of sea straits* pp. 171–189, Dordrecht: Springer.

Lindstrom, E., Lukas, R., Fine, R., Firing, E., Godfrey, S., Meyers, G., & Tsuchiya, M. (1987). The western equatorial Pacific Ocean circulation study. *Nature*, *330*(6148), 533–537.

Mackey, D., O'Sullivan, J. O., & Watson, R. (2002). Iron in the western Pacific: A riverine or hydrothermal source for iron in the equatorial undercurrent? *Deep Sea Research Part I: Oceanographic Research Papers*, *49*(5), 877–893.

Marin, F., Kestenare, E., Delcroix, T., Durand, F., Cravatte, S., Eldin, G., & Bourdalle-Badie, R. (2010). Annual reversal of the equatorial intermediate current in the Pacific: Observations and model diagnostics. *Journal of Physical Oceanography*, *40*(5), 915–933.

McCreary, J. P., & Lu, P. (1994). Interaction between the subtropical and equatorial ocean circulations: The subtropical cell. *Journal of Physical Oceanography*, *24*(2), 466–497.

Melet, A., Gourdeau, L., Kessler, W. S., Verron, J., & Molines, J.-M. (2010a). Thermocline circulation in the Solomon Sea: A modeling study*. *Journal of Physical Oceanography*, *40*(6), 1302–1319.

Melet, A., Gourdeau, L., & Verron, J. (2010b). Variability in Solomon Sea circulation derived from altimeter sea level data. *Ocean dynamics*, *60*(4), 883–900.

Melet, A., Gourdeau, L., Verron, J., & Djath, B. (2013). Solomon Sea circulation and water mass modifications: Response at ENSO time-scales. *Ocean Dynamics*, *63*(1), 1–19.

Melet, A., Verron, J., Gourdeau, L., & Koch-Larrouy, A. (2011). Equatorward pathways of Solomon Sea water masses and their modifications. *Journal of Physical Oceanography*, *41*(4), 810–826.

Murray, S., Lindstrom, E., Kindle, J., & Weeks, E. (1995). Transport through Vitiaz Strait. *WOCE notes*, *7*(1), 21–23.

Paduan, J. D., & Washburn, L. (2013). High-frequency radar observations of ocean surface currents. *Annual review of marine science*, *5*, 115–136.

Pennington, J. T., Mahoney, K. L., Kuwahara, V. S., Kolber, D. D., Calienes, R., & Chavez, F. P. (2006). Primary production in the eastern tropical Pacific: A review. *Progress in Oceanography*, *69*(2), 285–317.

Qin, X., Menviel, L., Sen Gupta, A., & Sebille, E. (2016). Iron sources and pathways into the Pacific equatorial undercurrent. *Geophysical Research Letters*, *43*, 9843–9851. https://doi.org/10.1002/2016GL070501

Qu, T., & Lindstrom, E. J. (2002). A climatological interpretation of the circulation in the western south Pacific. *Journal of Physical Oceanography*, *32*(9), 2492–2508.

Qu, T., & Lindstrom, E. J. (2004). Northward intrusion of Antarctic Intermediate Water in the western Pacific. *Journal of Physical Oceanography*, *34*(9), 2104–2118.

Qu, T., Mitsudera, H., & Yamagata, T. (1998). On the western boundary currents in the Philippine Sea. *Journal of Geophysical Research*, *103*(C4), 7537–7548.

Radic, A., Lacan, F., & Murray, J. W. (2011). Iron isotopes in the seawater of the equatorial Pacific Ocean: New constraints for the oceanic iron cycle. *Earth and Planetary Science Letters*, *306*(1-2), 1–10.

Reid Jr, J. L. (1965). Intermediate waters of the Pacific Ocean (*Tech. re.*): Scripps Institution of Oceanography La JOLLA CA.

Rio, M.-H., Mulet, S., & Picot, N. (2014). Beyond GOCE for the ocean circulation estimate: Synergetic use of altimetry, gravimetry, and in situ data provides new insight into geostrophic and Ekman currents. *Geophysical Research Letters*, *41*, 8918–8925. https://doi.org/10.1002/2014GL061773

Ryan, J. P., Ueki, I., Chao, Y., Zhang, H., Polito, P. S., & Chavez, F. P. (2006). Western Pacific modulation of large phytoplankton blooms in the central and eastern equatorial Pacific. *Journal of Geophysical Research*, *111*, G02013. https://doi.org/10.1029/2005JG000084

SPICE Community (2012). Naming a western boundary current from Australia to the Solomon Sea. *CLIVAR Newsletter Exchanges No. 58*, *17*(1), 28.

Santiago-Mandujano, F., & Firing, E. (1990). Mixed-layer shear generated by wind stress in the central equatorial Pacific. *Journal of physical oceanography*, *20*(10), 1576–1582.

Slemons, L. O., Murray, J. W., Resing, J., Paul, B., & Dutrieux, P. (2010). Western Pacific coastal sources of iron, manganese, and aluminum to the equatorial undercurrent. *Global Biogeochemical Cycles*, *24*, GB3024. https://doi.org/10.1029/2009GB003693

Slemons, L., Paul, B., Resing, J., & Murray, J. W. (2012). Particulate iron, aluminum, and manganese in the Pacific equatorial undercurrent and low latitude western boundary current sources. *Marine Chemistry*, *142*, 54–67.

Smith, N., Kessler, W. S., Cravatte, S. E., Sprintall, J., Wijffels, S. E., Cronin, M. F., et al. (2019). Tropical Pacific observing system. *Frontiers in Marine Science*, *6*, 31.

Smith, W. H., & Sandwell, D. T. (1997). Global sea floor topography from satellite altimetry and ship depth soundings. *Science*, *277*(5334), 1956–1962.

Sokolov, S., & Rintoul, S. (2000). Circulation and water masses of the southwest Pacific: WOCE section P11, Papua New Guinea to Tasmania. *Journal of Marine Research*, *58*(2), 223–268.

Srinivasan, K., McWilliams, J. C., Renault, L., Hristova, H. G., Molemaker, J., & Kessler, W. S. (2017). Topographic and mixed layer sub-mesoscale currents in the near-surface southwestern tropical Pacific. *Journal of Physical Oceanography*, *47*(6), 1221–1242.

Talley, L. D., & Sprintall, J. (2005). Deep expression of the Indonesian Throughflow: Indonesian intermediate water in the South Equatorial Current. *Journal of Geophysical Research*, *110*, C10009. https://doi.org/10.1029/2004JC002826

Tsuchiya, M. (1968). Upper waters of the intertropical Pacific Ocean. *Johns Hopkins Oceanographic Studies*, *4*, 50p.

Tsuchiya, M. (1981). The origin of the Pacific equatorial 13°C water. *Journal of Physical Oceanography*, *11*(6), 794–812.

Tsuchiya, M. (1991). Flow path of the Antarctic Intermediate Water in the western equatorial South Pacific Ocean. *Deep Sea Research Part A. Oceanographic Research Papers*, *38*, S273–S279.

Tsuchiya, M., Lukas, R., Fine, R. A., Firing, E., & Lindstrom, E. (1989). Source waters of the Pacific equatorial undercurrent. *Progress in Oceanography*, *23*(2), 101–147.

Wentz, F., Scott, J., Hoffman, R., Leidner, M., Atlas, R., & Ardizzone, J. (2015). Remote sensing systems Cross-Calibrated Multi-Platform (CCMP) 6-hourly ocean vector wind analysis product on 0.25 deg grid, Version 2.0, 2012-2014. Remote Sensing Systems, Santa Rosa, CA. Available online at www.remss.com/measurements/ccmp. Accessed 23 Oct 2017.

Zilberman, N., Roemmich, D., & Gille, S. (2013). The mean and the time variability of the shallow meridional overturning circulation in the tropical South Pacific Ocean. *Journal of Climate*, *26*(12), 4069–4087.